


Spin Dynamics of the Carr-Purcell-Meiboom-Gill Sequence in Time-Dependent Magnetic Fields

Martin D. Hürlimann,^{*} Shin Utsuzawa,[†] and Chang-Yu Hou[‡]
 Schlumberger-Doll Research, Cambridge, Massachusetts 02139, USA

 (Received 21 March 2019; revised manuscript received 25 July 2019; published 28 October 2019)

We analyze the effects of time-dependent magnetic and rf fields on the spin dynamics of the Carr-Purcell-Meiboom-Gill sequence. The analysis is based on the decomposition of the magnetization into the eigenmodes of the propagator of a single refocusing cycle. For sufficiently slow changes in the external fields, the magnetization follows the changing eigenmodes adiabatically. This results in echo amplitudes that show regular modulations with time. Faster field changes can induce transitions between the eigenmodes. Such nonadiabatic behavior occurs preferentially at particular offsets of the Larmor frequency from the rf frequency where the eigenmodes become nearly degenerate. We introduce the instantaneous adiabaticity parameter $\mathcal{A}(t)$ that accurately predicts the crossover from the adiabatic to the nonadiabatic regime and allows the classification of field fluctuations. $\mathcal{A}(t)$ is determined solely by the properties of a single refocusing cycle under static conditions and the instantaneous value of the field offset and its temporal derivative. The analytical results are compared with numerical simulations.

DOI: [10.1103/PhysRevApplied.12.044061](https://doi.org/10.1103/PhysRevApplied.12.044061)

I. INTRODUCTION

In the common implementation of NMR measurements, a significant effort is spent on ensuring that the applied magnetic field B_0 across the sample is both spatially and temporally as uniform as possible. However, in practice, some degree of field inhomogeneities are always present. In fact, there are a number of applications where field nonuniformities are large and unavoidable. A prime example is *ex situ* NMR [1] that includes NMR well logging [2] where the NMR sensor is moved across geological samples that are located outside the instrument.

Here we study the impact of temporal fluctuations of B_0 on the spin dynamics of the Carr-Purcell-Meiboom-Gill (CPMG) sequence [3,4]. This sequence is a basic building block in many NMR measurement schemes where significant field inhomogeneities are present. Applications include sensitivity enhancement [5] and the monitoring of dynamic processes such as relaxation and diffusion [6]. The CPMG sequence is also widely used to suppress general environmental decoherence in quantum computations, with the goal towards fault tolerance [7,8].

For complex systems with multiexponential decays, it is generally necessary to acquire large numbers of echoes with short echo spacings, t_E , to cover the entire range of relaxation times. Even in simple system, it can be beneficial to acquire many echoes with short t_E values, as it

enables an increase in the effective signal-to-noise ratio (SNR) by averaging the response over adjacent echoes. We are here interested in the case when the field fluctuations are slow on the time scale of the echo spacing, but when the overall amplitude over the entire CPMG train can approach or exceed B_1 , the strength of the rf field. The field fluctuations are considered to be slow when $(d/dt)B_0(t) \ll B_1/t_E$.

The carrier frequency of the rf pulses, ω_{rf} , is set to fulfill the Larmor condition $\omega_{\text{rf}} = \gamma B_0$ at the beginning of the sequence. Here γ is the gyromagnetic ratio. When B_0 fluctuates during the CPMG sequence, the pulses do not fulfill the Larmor condition exactly anymore. As a consequence, the refocusing pulses do not act anymore as perfect 180° pulses in the transverse plane. Naively, one might expect that these imperfections gradually accumulate and induce a steady reduction of the echo amplitudes. However, as is clearly apparent in numerical simulations of the spin dynamics in Sec. III, the observed behavior is more interesting. The resulting evolution of the magnetization of the spin echoes typically shows systematic structures with oscillations and abrupt changes. An example has been published earlier by Speier *et al.* [9].

The purpose of this Paper is to develop the underlying theory and explain this behavior. This is relevant in many different applications for the development of new sensors and the analysis of measurements. We illustrate this for the application of NMR well logging [2]. In this technique, the NMR sensor contains a magnet array and a rf coil system that is lowered into a borehole to investigate the fluid in the earth formation surrounding the borehole. The basic

^{*}mhurlimann@gmail.com

[†]SUtsuzawa@slb.com

[‡]CHou2@slb.com

NMR measurement consists of a CPMG sequence. The detected amplitude and decay time are related to the porosity and pore size, respectively. These quantities are of high value as they can be used to infer the fluid content and the transport properties of the earth formation. To optimize the efficiency of the data collection, the relaxation measurements are typically performed while the sensor is moving along the borehole.

As the sample is located outside the sensor, the magnetic and rf fields applied to the sample in this inside-out configuration are nonuniform. When measurements are conducted with a moving sensor, field inhomogeneities along the direction of motion are particularly problematic. As the sensor is moved across the sample, these spatial inhomogeneities translate into temporal field fluctuations, $\Delta B_0(t)$ and $\Delta B_1(t)$, at a given sample location. Such field fluctuations modify the CPMG spin dynamics and interfere with the desired relaxation measurement.

Field inhomogeneities along the direction of motion can be reduced by elongating the sensor, that includes the magnet array and rf coils, and by designing appropriate end corrections. In practical implementations, there are limits imposed on the overall sensor length; and the magnet array is likely constructed from a set of discrete blocks of permanent magnets and the rf coils from discrete wires. A key design criterion is the acceptable amplitude and profile of residual field inhomogeneity along the direction of motion, $\Delta B_0(z)$ or $\Delta B_1(z)$, to ensure that the relaxation measurement is not dominated by these motion effects. The derivation of this criterion requires an understanding of the impact of temporal field fluctuations on the CPMG spin dynamics.

Furthermore, borehole roughness can induce sensor motion perpendicular to the intended direction. As discussed above, the inhomogeneity of the magnetic field is minimized along the intended direction of motion, but the field is generally less uniform in a perpendicular direction. Such lateral motion can therefore induce significant additional temporal field fluctuations. It is common to monitor this type of motion with an accelerometer. To assess the level of lateral motion that can be tolerated without jeopardizing the quality of the NMR relaxation measurement, it is again essential to understand the impact of temporal fluctuations on the magnetization decay.

For the uncoupled spins considered here, the spin dynamics reduces essentially to a classical problem. The evolution of the magnetization, the expectation value of the angular-momentum operator, follows the standard electromagnetic equation that relates the change of the magnetic moment to the applied torque. Therefore, the magnetization follows the Bloch equations. To gain a more general insight into the impact of time-dependent fields, we use the concept of rotation operators to account for the influence of external magnetic fields and rf pulses. The combined effect of the individual rotation operators describing the

distinct intervals of a single CPMG cycle can be described again simply by a unitary operation. In the continuous limit when the external fields vary slowly compared to the echo spacing, we show that we can define an effective Hamiltonian to describe the evolution for the expectation value of the angular-momentum operator. As becomes transparent through our derivations, the identification of the effective Hamiltonian to describe such a classical evolution allows us to apply relevant techniques from quantum mechanics to obtain general results. One should, however, keep in mind that the interpretation of the eigenstates and eigenvalues in our problem is different from those in the true quantum-mechanical descriptions.

The Paper is organized as follows. The theory is presented in Sec. II. In Sec. III we present numerical simulations based on the Bloch equations that are compared with the theoretical results. This is followed by the conclusion in Sec. IV.

The theoretical analysis in Sec. II proceeds in two steps. We first derive the average Hamiltonian that describes a single refocusing cycle for an arbitrary off-resonance condition and obtain the eigenmodes. In the second step, we consider the response under this average Hamiltonian when it becomes time dependent. In the adiabatic regime applicable to sufficiently slow fluctuations, the evolution of the magnetization follows the eigenmodes of the instantaneous average Hamiltonian. Simple analytical expressions are obtained for this regime. We then derive the condition for the validity of the adiabatic regime. We introduce the instantaneous adiabaticity parameter $\mathcal{A}(t)$ that quantitatively predicts the extent of the adiabatic regime and the occurrence of nonadiabatic events. It is found that nonadiabatic events are typically confined to small regions of offset frequencies where the field fluctuations are able to induce transitions between the eigenmodes. In Sec. II G, the analysis is generalized to the treatment of fluctuations in the amplitudes of both B_0 and B_1 .

In Sec. III, we compare the analytical results obtained in Sec. II with numerical simulations of the CPMG response in nonstationary B_0 fields. We demonstrate that the theoretical treatment is rather general and applicable to various forms of field fluctuations. We present detailed comparison between theory and numerical simulation for linear ramp, harmonic motion, and bilinear field variations. We also study the dependence on the amplitude and rate of change of the fluctuations.

II. THEORY

A. Introduction

In this section, we develop the theory that describes the response of the CPMG sequence under a time-varying magnetic field, $B_0(t)$, as shown in Fig. 1. After the initial excitation pulse, the pulse sequence consists of a long string of rf pulses of duration t_p that are equally spaced

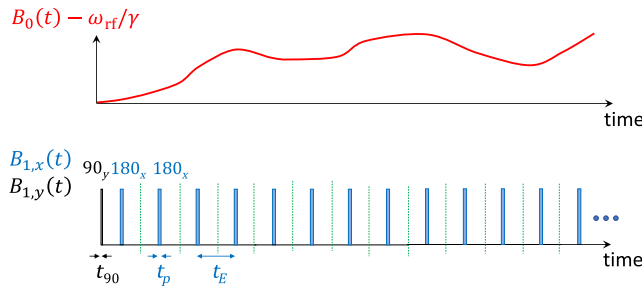


FIG. 1. Basic CPMG sequence with time-dependent B_0 field. The refocusing pulses are shown in blue and are assumed to have phase 0 and duration t_p . The excitation pulse with phase $\pi/2$ is shown in black and has a duration of t_{90} . The dotted lines show the positions of the nominal echo centers, separated by the echo spacing t_E .

by the echo spacing t_E . We are interested in the resulting magnetization \vec{M}_k at the nominal echo locations $t_k = kt_E$. We make the assumption that we deal with noninteracting spin-1/2 nuclei and for simplicity, we neglect T_1 and T_2 relaxation.

The relevant Hamiltonian in the rotating frame of the carrier frequency of the rf pulses, ω_{rf} , is given by

$$\mathcal{H} = -\hbar\gamma \{ [B_0(t) - \omega_{\text{rf}}/\gamma] I_z + B_{1,x}(t) I_x + B_{1,y}(t) I_y \}. \quad (1)$$

This simple form of the Hamiltonian is applicable for many practical applications. When the Hamiltonian also contains sizeable dipolar terms (see, for example, the solid-state NMR application discussed in Ref. [10]) a more detailed treatment is required that falls beyond the scope of the current work.

Both the longitudinal and transverse terms in Eq. (1) are time dependent, but on a different time scale. As mentioned in the introduction, we assume that the field B_0 varies only slowly compared to the echo spacing, t_E . In contrast, the rf terms represent short pulses of duration t_p that are repeated many times with a period of t_E . This separation of time scales allows us to proceed in two steps. We first deal with the fast time dependence of the rf pulses using average Hamiltonian theory [11,12] and then consider the impact of the slower variation of $B_0(t)$ on this average Hamiltonian.

In the first step, presented in Sec. II B, we ignore the time dependence of B_0 and consider only the effect of the periodically applied refocusing pulses. The average Hamiltonian theory is well suited for this analysis. The Hamiltonian is periodic in time and also fulfills the requirement that the generated signal is stroboscopically sampled between the refocusing pulse, synchronized with the time dependence of the Hamiltonian. The average Hamiltonian theory provides an analysis of the echo-to-echo propagator and is used previously for the study of the CPMG sequence with large static field inhomogeneities [13]. We give analytical solutions for the average Hamiltonian for

an arbitrary value of B_0 and diagonalize it. This allows us to expand the magnetization into three eigenstates.

The time dependence of $B_0(t)$ is then considered in Sec. II C. This can be viewed as a generalized treatment of the Landau-Zener problem [14,15]. The dynamics of $B_0(t)$ has a minor impact on the instantaneous eigenstates of the average Hamiltonian derived for the static B_0 and the corrections are derived to first order. We then show that for sufficiently slow variations of $B_0(t)$, the magnetization follows the instantaneous eigenstates adiabatically and we obtain analytical solutions for this case. Next, we derive the condition for adiabaticity and introduce the adiabaticity parameter \mathcal{A} . We show that this parameter has a strong sensitivity on the instantaneous offset frequency of the Larmor frequency from the rf frequency, $\gamma B_0(t) - \omega_{\text{rf}}$. Nonadiabatic events that cause transitions between the eigenstates are typically confined to small regions of offset frequency.

B. Average Hamiltonian

In the first step of the analysis, we derive the average Hamiltonian \mathcal{H}_{ave} for arbitrary (but time-independent) values of B_0 and B_1 .

It is useful to start the analysis by listing the key parameters that control the spin dynamics of this problem. There are three important frequencies.

1. ω_{rf} , the carrier frequency of the rf pulses that is under control of the experimenter.
2. $\omega_0(t) \equiv \gamma B_0(t) - \omega_{\text{rf}}$, the deviation of the instantaneous Larmor frequency from ω_{rf} that is proportional to the applied field.
3. $\omega_1 \equiv \gamma B_{1,\perp}/2$, the nominal nutation frequency of the refocusing pulses that is proportional to the amplitude of the applied linearly polarized rf field, $B_{1,\perp}$.

It is convenient to normalize the frequencies with the nominal nutation frequency $\omega_{1,\text{nom}}$ to make them dimensionless:

$$\tilde{\omega}_0(t) \equiv \frac{\omega_0(t)}{\omega_{1,\text{nom}}}, \quad (2)$$

$$\tilde{\omega}_1 \equiv \frac{\omega_1}{\omega_{1,\text{nom}}}. \quad (3)$$

The nominal nutation frequency is related to the duration of the perfect refocusing pulse on resonance, t_{180} , by $\omega_{1,\text{nom}} t_{180} = \pi$. In addition, we use the normalized time τ in units of t_E :

$$\tau \equiv \frac{t}{t_E}. \quad (4)$$

1. Effective rotation describing echo-to-echo propagator

For the case of noninteracting spins, \mathcal{H}_{ave} can be obtained exactly and does not require a Magnus expansion.

The refocusing cycle of the basic CPMG sequence consists of three subsequent intervals (see Fig. 2): a free-precession interval of duration $(t_E - t_p)/2$, followed by the rf pulse of duration t_p , and followed by a second free-precession interval of identical duration $(t_E - t_p)/2$. Each of these intervals acts as a rotation on the magnetization. The free-precession intervals correspond to rotations around \hat{z} with an angle $\beta_1 = \omega_0(t_E - t_p)/2$, while the rf pulse acts as a rotation around $(\omega_1\hat{x} + \omega_0\hat{z})/\sqrt{\omega_0^2 + \omega_1^2}$ with an angle $\sqrt{\omega_0^2 + \omega_1^2}t_p$. The net effect of these three subsequent rotations is a single effective rotation characterized by its rotation axis \hat{n} and rotation angle α . The relevant Euler parameters $[\hat{n} \sin(\alpha/2), \cos(\alpha/2)]$ can be calculated efficiently using quaternions [16–18].

The properties of the effective rotation describing the average Hamiltonian for a refocusing cycle of the CPMG sequence with static B_0 field (see Fig. 2) are given by Ref. [13]:

$$n_{\perp} = \frac{1}{\Delta} \frac{\omega_1}{\Omega} \sin \beta_2, \quad (5)$$

$$n_z = \frac{1}{\Delta} \left[\sin \beta_1 \cos \beta_2 + \frac{\omega_0}{\Omega} \cos \beta_1 \sin \beta_2 \right], \quad (6)$$

$$\cos\left(\frac{\alpha}{2}\right) = \cos \beta_1 \cos \beta_2 - \frac{\omega_0}{\Omega} \sin \beta_1 \sin \beta_2, \quad (7)$$

where

$$\Omega = \sqrt{\omega_0^2 + \omega_1^2}, \quad (8)$$

$$\beta_1 = \omega_0(t_E - t_p)/2, \quad (9)$$

$$\beta_2 = \Omega t_p/2, \quad (10)$$

$$\Delta^2 = \left[\frac{\omega_1}{\Omega} \sin \beta_2 \right]^2 + \left[\sin \beta_1 \cos \beta_2 + \frac{\omega_0}{\Omega} \cos \beta_1 \sin \beta_2 \right]^2. \quad (11)$$

The azimuthal angle ε of \hat{n} (see Fig. 2) for the static case is identical to the phase of the refocusing pulses, i.e., $\varepsilon = 0$ for x and $\varepsilon = \pi/2$ for y -refocusing pulses.

Equations (5)–(7) show that the angle α and the direction of the axis \hat{n} describing the average Hamiltonian have a nontrivial dependence on the offset frequency ω_0 . This is further illustrated in Fig. 3 for two cases of echo spacings.

The propagator for the magnetization from the $N - 1$ th to the N th echo is the rotation on the Bloch sphere around the axis \hat{n} with angle α :

$$\vec{M}^{(N)} = \mathcal{R}_{\hat{n}}(\alpha) \{ \vec{M}^{(N-1)} \}. \quad (12)$$

In the rotating frame of the rf frequency ω_{rf} , the rotation can be represented by a 3×3 matrix with the elements R_{jk} ($j, k = x, y$, or z) given by $R_{jk} = n_j n_k + (\delta_{jk} - n_j n_k) \cos(\alpha) - \epsilon_{jkl} n_l \sin(\alpha)$. Here δ_{jk} is the Kronecker delta, ϵ_{jkl} is the Levi-Civita symbol, and n_j is the projection of \hat{n} onto the axis \hat{j} .

Equivalently, the rotation matrix in Eq. (12) can be cast into the form of the SO(3) unitary transformation:

$$\mathcal{R}_{\hat{n}}(\alpha) = \exp \left\{ -i\alpha \hat{n} \cdot \vec{\mathcal{S}} \right\}. \quad (13)$$

Here $\vec{\mathcal{S}} = (\mathcal{S}_1, \mathcal{S}_2, \mathcal{S}_3)$ is a vector whose components are the three real 3×3 antisymmetric matrices \mathcal{S}_k representing generators of rotations with respect to three axes in the Cartesian coordinate system. The matrix elements of \mathcal{S}_k are given by $(\mathcal{S}_k)_{ij} = -i\epsilon_{ijk}$.

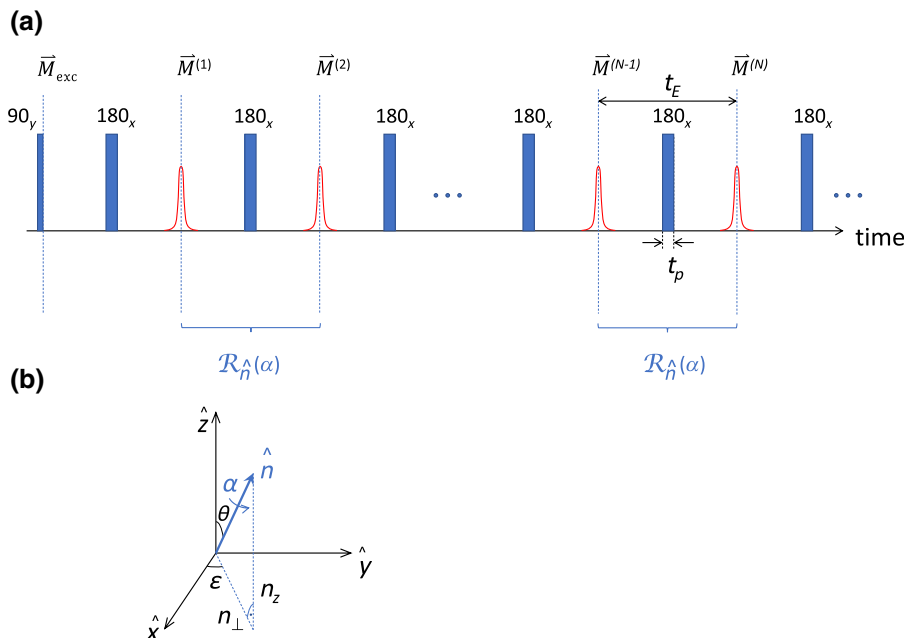


FIG. 2. (a) CPMG sequence with indication of the echo-to-echo propagator $\mathcal{R}_{\hat{n}}(\alpha)$. (b) Definition of the parameters used to describe the echo-to-echo $\mathcal{R}_{\hat{n}}(\alpha)$ propagator in terms of the rotation axis \hat{n} and rotation angle α .

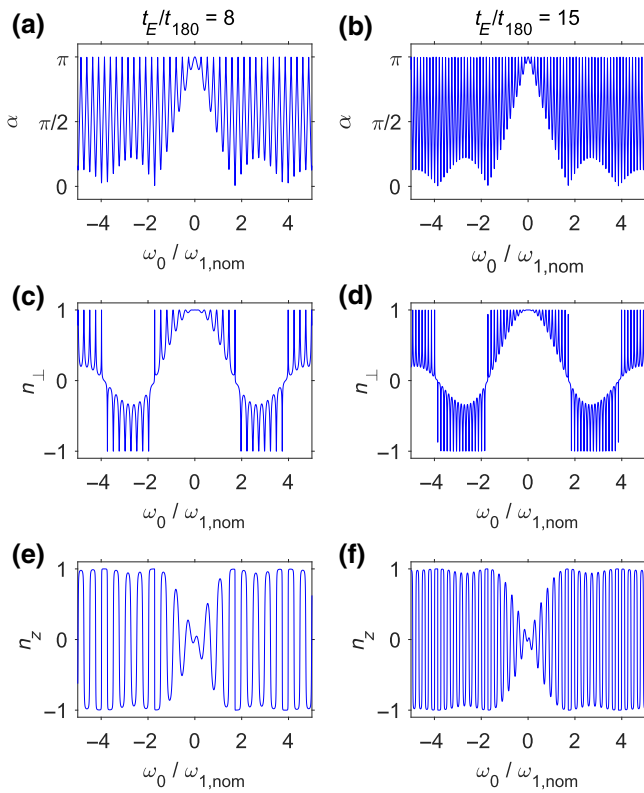


FIG. 3. Properties of the effective rotation representing the average Hamiltonian for two different echo spacings, $t_E/t_{180} = 8$ [(a),(c), and (e)] and $t_E/t_{180} = 15$ [(b),(d), and (f)], respectively. The top panels (a),(b) show the angle α as a function of $\tilde{\omega}_0$ obtained from Eq. (7). Note that given the equivalence of the rotations $\{\hat{n}, \alpha\}$ and $\{-\hat{n}, \alpha \pm \pi\}$, it is always possible to choose $0 \leq \alpha \leq \pi$. Panels (c) and (d) show the transverse component, Eq. (5), and (e) and (f) show the longitudinal component, Eq. (6), of the axis \hat{n} .

The \mathcal{S}_k matrices also appear in the representation of uncoupled spin $S = 1$ particles, which can be shown by a simple basis transformation. By rewriting the rotation matrix in the exponential form, it becomes transparent that in the continuous limit, the evolution of the magnetization from echo to echo in a CPMG sequence is equivalent to that of a spin $S = 1$ particle subjected to a continuous average magnetic field, $\mathcal{B}_{\text{ave}} = (\alpha/\gamma t_E)\hat{n}$, with the average Hamiltonian reading as

$$\mathcal{H}_{\text{ave}} \equiv \hbar\gamma\mathcal{B}_{\text{ave}} \cdot \vec{S} = \hbar\frac{\alpha}{t_E}\hat{n} \cdot \vec{S}. \quad (14)$$

It is, however, prudent to keep in mind that despite the mathematical similarity to a fully quantum-mechanical treatment, our eigenstates describe the directly observable magnetization of the nuclei ensemble. This is unlike in quantum mechanics where the eigenstates correspond to wave functions that are subjected to the probability interpretation.

2. Eigenmodes of the average Hamiltonian

It is straightforward to solve the eigenvalue problem of the average Hamiltonian of Eq. (14),

$$\mathcal{H}_{\text{ave}}\hat{v}_k = E_k\hat{v}_k. \quad (15)$$

There are three eigenmodes labeled by $k = -1, 0, +1$. The eigenvalues E_k are given by

$$E_k = k\frac{\hbar\alpha}{t_E}. \quad (16)$$

It is critical to note that the energy level associated with the $k = 0$ mode is always zero. This is a general topological property of any rotation: the component of magnetization along the axis of rotation is always preserved. Figure 4 shows the corresponding energy-level diagram (in frequency units) as a function of offset frequency $\tilde{\omega}_0$ assuming $\omega_1 = \omega_{1,\text{nom}}$. The levels for $k = \pm 1$ are separated from the $k = 0$ mode by π/t_E near $\omega_0 = 0$, but are nearly degenerate with a much smaller gap at other offsets such as in the neighborhood of $\omega_0 = 1.7\omega_{1,\text{nom}}$.

The three eigenvectors \hat{v}_k are controlled by the direction of the axis of rotation, \hat{n} , and are independent of α . In cylindrical coordinates of \hat{n} (see Fig. 2), they are given by

$$\hat{v}_0 = \hat{n} = \begin{pmatrix} n_{\perp} \cos \varepsilon \\ n_{\perp} \sin \varepsilon \\ n_z \end{pmatrix}; \quad (17)$$

$$\hat{v}_{+1} = \frac{-i}{\sqrt{2}} \begin{pmatrix} n_z \cos \varepsilon - i \sin \varepsilon \\ n_z \sin \varepsilon + i \cos \varepsilon \\ -n_{\perp} \end{pmatrix}; \quad (18)$$

$$\hat{v}_{-1} = \frac{i}{\sqrt{2}} \begin{pmatrix} n_z \cos \varepsilon + i \sin \varepsilon \\ n_z \sin \varepsilon - i \cos \varepsilon \\ -n_{\perp} \end{pmatrix}. \quad (19)$$

Note that the eigenvector \hat{v}_0 points along the axis of rotation, \hat{n} , and \hat{v}_{+1} and \hat{v}_{-1} are complex conjugates of each other. As expected, the eigenvectors fulfill the orthonormal condition $\hat{v}_k \cdot \hat{v}_l^* = \delta_{kl}$.

3. Decomposition into CPMG and CP magnetizations

Given the eigenmodes of the average Hamiltonian, it is straightforward to obtain an analytical expression for the magnetization at the N th echo, $\vec{M}^{(N)}$ by decomposing the magnetization into the eigenmodes. For each mode, the echo-to-echo propagator is a simple phase factor $e^{-ik\alpha}$:

$$\vec{M}^{(N)} = \sum_{k=-1}^{+1} a_k e^{-ikN\alpha} \hat{v}_k. \quad (20)$$

For the static case, the mode amplitudes a_k are determined by the projection of the initial magnetization after

the excitation pulse, \vec{M}_{exc} , onto the eigenvector \hat{v}_k :

$$a_k = \vec{M}_{\text{exc}} \cdot \hat{v}_k^*. \quad (21)$$

We generally refer to the $k = 0$ term as the CPMG magnetization, whereas we refer to the sum of the $k = \pm 1$ terms as the Carr-Purcell (CP) magnetization.

$$\vec{M}^{(N)} = \vec{M}_{\text{CPMG}} + \vec{M}_{\text{CP}}^{(N)}, \quad (22)$$

where

$$\vec{M}_{\text{CPMG}} = a_0 \hat{v}_0 = a_0 \hat{n}, \quad (23)$$

$$\vec{M}_{\text{CP}}^{(N)} = a_{-1} e^{ikN\alpha} \hat{v}_{-1} + a_{+1} e^{-ikN\alpha} \hat{v}_{+1}. \quad (24)$$

This notation is motivated by the fact that on resonance, the Carr-Purcell-Meiboom-Gill sequence [4] generates ideally only the CPMG component (i.e., $a_0 = 1$, $a_{\pm 1} = 0$), whereas the original Carr-Purcell sequence [3] generates only the CP component (i.e., $a_0 = 0$, $a_{\pm 1} = 1/\sqrt{2}$).

In general, the measured magnetization has contributions from both terms of Eq. (22). The CPMG term (23) has a number of special properties. It is always real and its phase factor is exactly unity. This term is therefore independent of the echo number N . Even in inhomogeneous fields, the magnetization associated with this term remains constant from echo to echo. Note that \vec{M}_{CPMG} can be extracted from $\vec{M}^{(N)}$ by a projection onto \hat{n} :

$$\vec{M}_{\text{CPMG}} = (\vec{M}^{(N)} \cdot \hat{n}) \hat{n}. \quad (25)$$

The $k = \pm 1$ terms in Eq. (20) that contribute to $\vec{M}_{\text{CP}}^{(N)}$ are, in general, complex. However, since the $k = -1$ term is the complex conjugate of the $k = +1$ term, the CP magnetization (24) is real, as any observed magnetization has to be. The phase of the CP magnetization evolves from echo to echo, but its magnitude in a homogeneous field is preserved. It can be extracted from $\vec{M}^{(N)}$ by a projection onto \hat{v}_{+1} or \hat{v}_{-1} :

$$|\vec{M}_{\text{CP}}| = \sqrt{2} |(\vec{M}^{(N)} \cdot \hat{v}_{\pm 1}^*)| = \sqrt{2} |a_{\pm 1}|. \quad (26)$$

In contrast to the CPMG magnetization, the CP magnetization is strongly affected by field inhomogeneities. In inhomogeneous fields, the values for α show a distribution, which leads to a distribution of the phase factor $e^{-ikN\alpha}$ in Eq. (20) for $k = \pm 1$. Consequently, $\vec{M}_{\text{CP}}^{(N)}$ in nonuniform fields dephases with increasing echo number. This is analogous to T_2^* dephasing in standard free-induction measurements in inhomogeneous fields. In most practical cases, $\vec{M}_{\text{CP}}^{(N)}$ decays quickly with N and the observable magnetization $\vec{M}^{(N)}$ is well approximated by \vec{M}_{CPMG} at high echo numbers. In grossly inhomogeneous fields as studied in Ref. [13] this occurs already after the second echo.

C. Time-dependent $B_0(t)$: time-dependent average Hamiltonian

In the previous section, we treat the time dependence of the rf field B_1 in the original Hamiltonian (1) using the average Hamiltonian approach for an arbitrary, but constant value of B_0 . We now take into account the time dependence of $\vec{B}_0(t)$. As mentioned in the introduction, we assume here that $d\tilde{\omega}_0/d\tau \ll 1$.

When B_0 and B_1 are time dependent, the propagator for each cycle can still be expressed in terms of a rotation operator. For each refocusing cycle j , we can still define an average Hamiltonian in the rotating frame associated with ω_{rf} with its corresponding eigenvectors and phase factors. However, the eigenvectors and eigenvalues now generally change from one refocusing cycle to the next. Formally, the evolution of magnetization for the dynamic case can be written as

$$\vec{M}^{(N)} = \mathcal{R}_{\hat{n}^{(N)}}(\alpha^{(N)}) \{ \mathcal{R}_{\hat{n}^{(N-1)}}(\alpha^{(N-1)}) \dots \dots \{ \mathcal{R}_{\hat{n}^{(1)}}(\alpha^{(1)}) (\vec{M}_{\text{exc}}) \} \dots \}. \quad (27)$$

As in Eq. (22) for the static case, we can still decompose the magnetization into corresponding CPMG and CP components at each cycle in the dynamic case. However, transitions between the CPMG and CP components now become possible from cycle to cycle, as the eigenmodes change.

The formal expression of magnetization evolution in Eq. (27) can be cast into the form in terms of the average Hamiltonians $\mathcal{H}_{\text{ave}}(\alpha^{(j)}, \hat{n}^{(j)})$ as:

$$\vec{M}^{(N)} = \mathcal{T} \left\{ \prod_{j=1}^N \exp \left[-i \frac{\mathcal{H}_{\text{ave}}(\alpha^{(j)}, \hat{n}^{(j)})}{\hbar} t_E \right] \right\} \vec{M}_{\text{exc}}, \quad (28)$$

where $\mathcal{T} \{ \dots \}$ is the time-ordered operator. The average Hamiltonian $\mathcal{H}_{\text{ave}}(\alpha^{(j)}, \hat{n}^{(j)})$ is still defined by Eq. (14), but with the rotation angle $\alpha^{(j)}$ and the rotation axis $\hat{n}^{(j)}$ now specified at each cycle. It operates on the observable magnetization.

To lowest order in $d\tilde{\omega}_0/d\tau$, $\alpha^{(j)}$ and $\hat{n}^{(j)}$ can be obtained from expressions (5)–(7) at the instantaneous values of ω_0 and ω_1 at the j th cycle. B_0 field variation during the refocusing cycle j leads to a small correction to the azimuthal angle ε that describes the direction of $\hat{n}_{\perp}^{(j)}$. To first order in $d\tilde{\omega}_0/d\tau$, the correction is given by

$$\delta\varepsilon^{(j)} = \frac{\pi}{8} \frac{t_E}{t_{180}} \frac{d\tilde{\omega}_0^{(j)}}{d\tau}. \quad (29)$$

There is no first-order correction to the angle $\alpha^{(j)}$ from its instantaneous value.

D. Slow fluctuation: Adiabatic regime

Now, the problem at hand is a particular case of evolution under a time-dependent Hamiltonian, which allows us to apply the mathematical tools and physical insights established in quantum mechanics to our classical problem. When the variations of magnetic fields and hence of the corresponding Hamiltonian are sufficiently slow, we expect that the evolution of the time-dependent eigenstates follows the instantaneous eigenstates of the Hamiltonian up to the dynamic phase and a geometric phase [19]. As a result, the general expression for the adiabatic evolution of the magnetization at the N th echo, Eq. (27), simplifies to

$$\vec{M}_{\text{adia}}^{(N)} = \sum_{k=-1}^{+1} \left(\vec{M}_{\text{exc}} \cdot \hat{v}_k^{(1)*} \right) \times \exp \left\{ -ik \sum_{j=1}^N \alpha^{(j)} + i \sum_{j=1}^{N-1} \Gamma_k^{(j)} \right\} \hat{v}_k^{(N)}. \quad (30)$$

Here, the term $\left(\vec{M}_{\text{exc}} \cdot \hat{v}_k^{(1)*} \right) = a_k^{(1)}$ is the initial amplitude of mode k . It depends on the initial magnetization after the excitation pulse, \vec{M}_{exc} and the eigenvector of the first refocusing cycle, $\hat{v}_k^{(1)}$. The term $\exp \left\{ -ik \sum_{j=1}^N \alpha^{(j)} \right\}$ accounts for the accumulated dynamic phase during all the refocusing cycles, while the term $\exp \left\{ i \sum_{j=1}^{N-1} \Gamma_k^{(j)} \right\}$ describes the accumulated geometric phase with $\Gamma_k^{(j)}$ given by Ref. [20]:

$$\Gamma_k^{(j)} = -\Im \left\{ \ln \left[\hat{v}_k^{(j)*} \cdot \hat{v}_k^{(j+1)} \right] \right\}, \quad (31)$$

where $\Im \{ \dots \}$ takes the imaginary part of the argument. In Eq. (30), the last term $\hat{v}_k^{(N)}$ is the eigenvector of the final refocusing cycle N . In the adiabatic limit, there are no transitions between CPMG and CP components.

For the particular interest of the CPMG ($k = 0$) component, the dynamic phase vanishes throughout the time evolution as E_0 is exactly zero for this component. Critically, the geometric phase also vanishes exactly as $\hat{v}_0^{(j)} = \hat{n}(t_j)$ is real for each refocusing cycle. We hence obtain the key result:

$$\vec{M}_{\text{CPMG,adia}}^{(N)} = \left[\vec{M}_{\text{exc}} \cdot \hat{n}(t_1) \right] \hat{n}(t_N) = a_0^{(1)} \hat{n}(t_N). \quad (32)$$

This result shows that in the adiabatic regime, the magnetization of the CPMG component only depends on the value of B_0 and B_1 at the beginning of the sequence and at the echo time of interest. It does not depend on the field variation between these points. In particular, for periodic variations when the field returns to its original value, the magnetization of the CPMG component also returns to its initial value. In contrast, the magnetization of the CP component retains a path dependence through both

the dynamic phase, $\phi_{\text{dyn}} = \sum_{j=1}^N \alpha^{(j)}$, and the geometric phase, $\phi_{\text{geo}} = \sum_{j=1}^{N-1} \Gamma_{\pm 1}^{(j)}$ in Eq. (30).

The results of Eqs. (30) and (31) are expressed in the rotating frame of the rf frequency ω_{rf} . In this case, the appearance of the geometric phase can be thought of as a manifestation of the generalized Coriolis effect as the direction of the eigenfunction changes with time. Alternatively, Garwood *et al.* [21] analyzed adiabatic pulses using a doubly rotating frame of reference where this effect manifests itself instead as an additional fictitious field that is proportional to the rate of change of the average field.

E. Adiabatic condition and beyond the adiabatic regime

To take full advantage of the Hamiltonian language, we now promote the magnetization evolution in Eq. (28) from discrete operations into the continuous formalism, such that

$$\vec{M}(t) = \exp \left[-\frac{i}{\hbar} \int_0^t \mathcal{H}_{\text{ave}}(t') dt' \right] \vec{M}_{\text{exc}}, \quad (33)$$

where the time-dependent Hamiltonian is given by

$$\mathcal{H}_{\text{ave}}(t) \equiv \hbar \gamma \mathcal{B}_{\text{ave}}(t) \cdot \vec{S} = \hbar \frac{\alpha(t)}{t_E} \hat{n}(t) \cdot \vec{S}. \quad (34)$$

As we discuss later, this continuous evolution formalism allows us to understand qualitatively (or quantitatively when the continuous limit is well justified) the transition between CPMG and CP modes in the dynamic cases.

The validity of the adiabatic evolution given by Eqs. (30) and (32) depends on how fast the magnetic field is changing. Following the arguments developed for standard fast passage experiments [22,23], the adiabatic condition requires that the direction of the average field (or here \hat{n}) has to change with a rate slower than the instantaneous nutation frequency. As long as the variations of magnetic fields do not accelerate or decelerate drastically, we can safely ignore the change of $\hat{n}(t)$ in the azimuthal direction and the rate of change of the direction of $\mathcal{B}_{\text{ave}}(t)$ is given by $d\theta/dt$. Here, θ (see Fig. 2) can be obtained by the relationships $n_{\perp} = \sin(\theta)$ and $n_z = \cos(\theta)$ from Eqs. (5) and (6). The effective nutation frequency is given by α/t_E . This results in the adiabatic condition:

$$\left| \frac{d\theta}{dt} \right| \ll \left| \frac{\alpha}{t_E} \right|. \quad (35)$$

It is also useful to consider the current problem as an example of a Landau-Zener type of problem [14,15,24,25]. As the offset frequency ω_0 increases from on resonance $\omega_0 = 0$ to a larger absolute value, the effective energy gap shown in Fig. 4 oscillates and reduces to near zero at certain values where a strong “diabatic” transition between

the CPMG and CP modes can occur. To quantify transitions between the CPMG and CP modes induced by the variations of magnetic fields, it is most convenient to use the continuous formalism for the magnetization evolution given in Eqs. (33) and (34). In the continuous limit, the adiabatic evolution of the magnetization reads as

$$\vec{M}_{\text{adia}}(t) = \sum_{k=-1}^{+1} [\vec{M}_{\text{exc}} \cdot \hat{v}_k^*(0)] \times \exp \left\{ -\frac{i}{\hbar} \int_0^t E_k(t') dt' + i\Gamma_k(t) \right\} \hat{v}_k(t), \quad (36)$$

with the geometric phase $\Gamma_k(t)$ given by Ref. [20]:

$$\Gamma_k(t) = i \int_0^t dt' \hat{v}_k^*(t') \cdot \partial_{t'} \hat{v}_k(t'). \quad (37)$$

Similar to the discrete case, the term $[\vec{M}_{\text{exc}} \cdot \hat{v}_k^*(0)]$ is the initial amplitude $a_k(0)$ of mode k at $t = 0$, the integral of E_k gives the dynamical phases, and $\hat{v}_k(t)$ is the eigenvector at the instantaneous time t .

As noted, Eq. (36) is only an approximate solution to the original effective Hamiltonian in Eq. (34) with the effective field $\mathcal{B}_{\text{ave}}(t)$ in the adiabatic limit. However, following the argument and derivation by Berry in Ref. [26], it is an exact solution to a related problem with a Hamiltonian of the same functional form but with a modified effective field \mathcal{B}_{mod} as

$$\gamma \mathcal{B}_{\text{mod}}(t) = \gamma \mathcal{B}_{\text{ave}}(t) + \hat{n}(t) \times \partial_t \hat{n}(t). \quad (38)$$

The modified field $\mathcal{B}_{\text{mod}}(t)$ consists of the sum of the original effective field $\mathcal{B}_{\text{ave}}(t)$ and the additional fictitious field proportional to $\hat{n}(t) \times \partial_t \hat{n}(t)$. This fictitious field is governed by the tangential variation of the rotation direction,

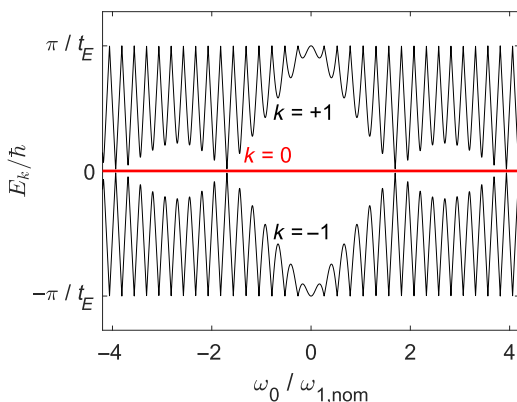


FIG. 4. Energy diagram for the average Hamiltonian \mathcal{H}_{ave} as a function of the normalized offset frequency $\tilde{\omega}_0 = \omega_0/\omega_{1,\text{nom}}$ with $\omega_1 = \omega_{1,\text{nom}}$. The energy level for the $k = 0$ level (also referred to as the CPMG level) is zero and is shown in red. Here we assume $t_E/t_{180} = 8.1$.

$\hat{n}(t)$ [or equivalently the direction of the effective field $\mathcal{B}_{\text{ave}}(t)$].

Some quick observations are worth mentioning here. First, a comparison of the magnitude of the fictitious field to that of the original effective field allows us to evaluate the validity of the adiabatic approximation. The magnitude of the fictitious field is $|d\theta/dt|$, while the magnitude of the original field is α/t_E . We thus recover the adiabatic condition stated in Eq. (35). Second and less directly, an inverted version of Eq. (38) can be used for the evaluation of transition between the CPMG and CP when the continuous limit is well justified, which we discuss in the Appendix.

F. Critical ramp rate $\nu_{0,\text{crit}}$ and adiabaticity parameter \mathcal{A}

The adiabatic condition in Eq. (35) is expressed in terms of the quantities $\{\theta, \alpha\}$ that refer to the direction and amplitude of the effective field $\mathcal{B}_{\text{ave}}(t)$. To relate the adiabatic condition more directly to the rate of change of the applied magnetic field B_0 , we rewrite the change of the direction of \hat{n} in terms of the rate of change of $\tilde{\omega}_0$ by

$$\frac{d\theta}{dt} = \frac{d\theta}{d\omega_0} \frac{d\omega_0}{dt} = \frac{1}{t_E} \frac{d\theta}{d\tilde{\omega}_0} \frac{d\tilde{\omega}_0}{d\tau}. \quad (39)$$

Here we assume that B_1 is constant in time. It is useful to introduce the critical ramp rate of $\nu_{0,\text{crit}}$ defined by

$$\nu_{0,\text{crit}} \equiv \frac{\alpha}{d\theta/d\tilde{\omega}_0}, \quad (40)$$

so that the adiabatic condition (35) becomes

$$\frac{d\tilde{\omega}_0}{d\tau} \ll \nu_{0,\text{crit}}. \quad (41)$$

The critical ramp rate is a dimensionless quantity that depends only on the static rotation properties of the refocusing cycle and can be calculated from Eqs. (5)–(7). Figure 5 shows the dependence of $\nu_{0,\text{crit}}$ on the offset frequency $\tilde{\omega}_0$. The critical ramp rate in Fig. 5 shows a high sensitivity on $\tilde{\omega}_0$ with pronounced minima near $\tilde{\omega}_0 = \pm 1.7$ and ± 3.9 . This is consistent with the energy-level diagram of Fig. 4 that shows that at these offsets, the energy splitting between the CPMG and CP levels nearly vanishes and transitions are easier to induce.

It is useful to introduce the adiabaticity parameter \mathcal{A} defined as the ratio of the critical ramp rate $\nu_{0,\text{crit}}$ and the dimensionless experimental ramp rate $d\tilde{\omega}_0/d\tau$:

$$\mathcal{A} \equiv \left| \frac{\nu_{0,\text{crit}}}{\frac{d\tilde{\omega}_0}{d\tau}} \right|. \quad (42)$$

The adiabatic condition (35) now becomes simply $\mathcal{A} \gg 1$.

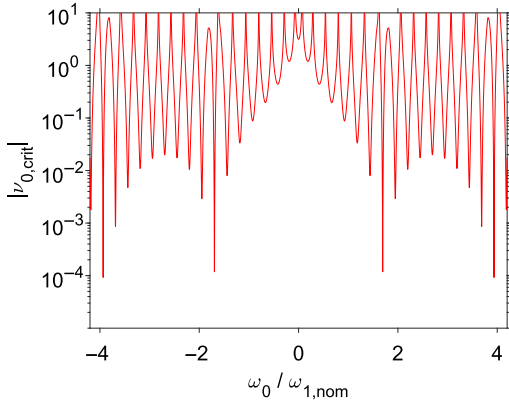


FIG. 5. Critical ramp rate $\nu_{0,\text{crit}}$ versus $\tilde{\omega}_0$ calculated from Eq. (40). Here we assume $\omega_1 = \omega_{1,\text{nom}}$ and $t_E/t_{180} = 8.1$.

G. Extension to time variable B_0 and B_1 fields

To obtain a better understanding of the origin of the minima in $\nu_{0,\text{crit}}$, it is instructive to consider the more general case when both B_0 and B_1 fields are time dependent, illustrated in Fig. 6. In this treatment, we neglect the temporal variation of B_1 throughout the duration of an individual rf pulse, but take into account the change of B_1 from one pulse to the next. In this case, the evolution is still described by Eq. (27) with the average Hamiltonian of the form Eq. (34) with the direction and amplitude of the effective field $\{\theta, \alpha\}$ given by Eqs. (5)–(7) and Eq. (29). These quantities now depend not only on the instantaneous value of $\tilde{\omega}_0(t)$ but also on $\tilde{\omega}_1(t)$, but otherwise the treatment carries through. Similarly, the expressions for the adiabatic regime, Eqs. (30) and (32), are still applicable when both B_0 and B_1 are fluctuating, as is the general form for the adiabatic condition Eq. (35).

However, the expression for the adiabaticity parameter \mathcal{A} in Eq. (42) has to be generalized to take into account the fluctuations of B_1 . Given that the nutation frequency of the pulses, $\omega_1 = \gamma B_{1,\perp}/2$, is now time dependent, it is essential to take this into account. In the general case, the temporal derivative of the angle θ has to be expanded into temporal derivatives of $\tilde{\omega}_0$ and $\tilde{\omega}_1$:

$$\frac{d\theta[\tilde{\omega}_0(\tau), \tilde{\omega}_1(\tau)]}{d\tau} = \frac{d\theta}{d\tilde{\omega}_0} \frac{d\tilde{\omega}_0}{d\tau} + \frac{d\theta}{d\tilde{\omega}_1} \frac{d\tilde{\omega}_1}{d\tau}. \quad (43)$$

It is useful to introduce now an additional critical ramp rate for B_1 , $\nu_{1,\text{crit}}$ that sets the scale of admissible B_1 variations within the adiabatic regime:

$$\nu_{1,\text{crit}} \equiv \frac{\alpha}{d\theta/d\tilde{\omega}_1}. \quad (44)$$

The generalized adiabaticity parameter now becomes

$$\frac{1}{\mathcal{A}} = \left| \frac{1}{\nu_{0,\text{crit}}} \frac{d\tilde{\omega}_0}{d\tau} + \frac{1}{\nu_{1,\text{crit}}} \frac{d\tilde{\omega}_1}{d\tau} \right|. \quad (45)$$

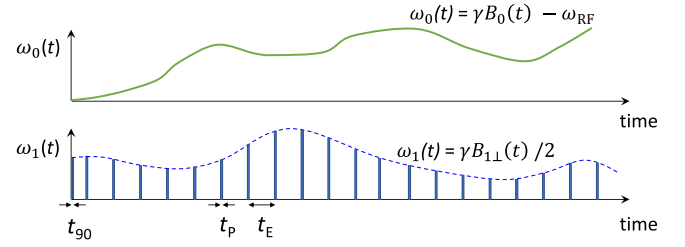


FIG. 6. General case of the CPMG sequence with fluctuating B_0 and B_1 fields, leading to time dependence of ω_0 and ω_1 .

With this generalized definition of the adiabaticity parameter, the adiabatic condition remains $\mathcal{A} \gg 1$.

Figure 7 shows the two critical ramp rates $\nu_{0,\text{crit}}$ and $\nu_{1,\text{crit}}$ as a function of $\tilde{\omega}_0$ and $\tilde{\omega}_1$. In addition, cross sections for $\omega_1 = \omega_{1,\text{nom}}$ are shown on the right panels.

The critical ramp rates $\nu_{0,\text{crit}}$ and $\nu_{1,\text{crit}}$ vanish at a discrete values of $(\tilde{\omega}_0, \tilde{\omega}_1)$ that are indicated by crosses in Fig. 7. They correspond to singular points where the propagator becomes exactly the unity operator. These singular points occur at [13]

$$(\tilde{\omega}_0, \tilde{\omega}_1)_{\text{singular}, l, m} = \left\{ \pm \frac{2(l-m)}{\frac{t_E}{t_{180}} - 1}, \sqrt{(2l)^2 - \left[\frac{2(l-m)}{\frac{t_E}{t_{180}} - 1} \right]^2} \right\}, \quad (46)$$

where l and m are integers with $l \leq m < lt_E/t_{180}$. For a unity operator, the nutation angle $\alpha = 0$. As a consequence, the CPMG and CP levels become degenerate leading to transitions between CPMG and CP modes.

When the $B_0 - B_1$ fluctuation corresponds to a trajectory in the $(\tilde{\omega}_0, \tilde{\omega}_1)$ plane that intersects any of these singular points, the adiabaticity parameter \mathcal{A} momentarily becomes 0 and the overall spin dynamics cannot be adiabatic. On trajectories that do not intersect but get close to these points, \mathcal{A} drops, but for sufficiently slow passage around these points it is possible to prevent transitions between the CPMG and CP levels. The singular points for a particular value of l lie on a circle of radius $2l$ in the $\tilde{\omega}_0 - \tilde{\omega}_1$ plane. When the B_1 field is fixed at its nominal value (i.e., $\tilde{\omega}_1 = 1$), the trajectory of any B_0 fluctuation corresponds to a straight horizontal line in the $(\tilde{\omega}_0, \tilde{\omega}_1)$ plane that intersects these circles at $\tilde{\omega}_0 = \pm\sqrt{4l^2 - 1} = \pm(1.73, 3.87, 5.92, \dots)$. This explains why the pronounced minima in $\nu_{\text{crit},0}$ and $\nu_{\text{crit},1}$ are observed in Figs. 5 and 7 occur near these offset frequencies.

III. COMPARISON OF THEORY WITH NUMERICAL SIMULATIONS

To test the validity of the analytical results, we compare the analytical results with numerical simulations. We use

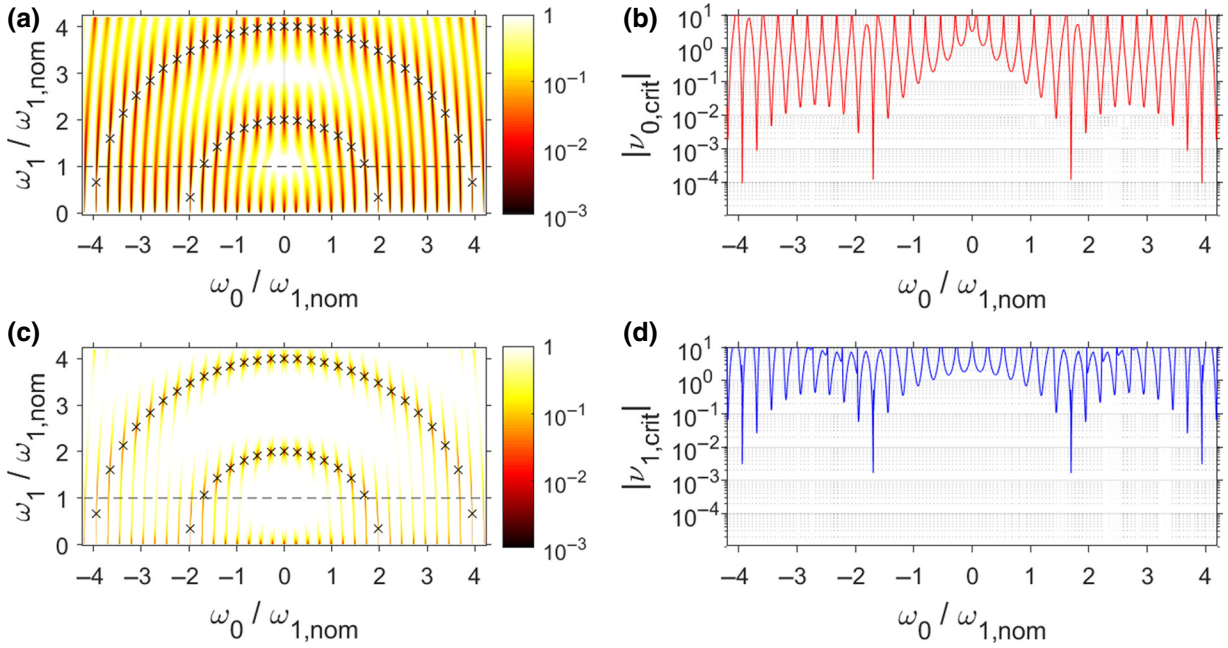


FIG. 7. Critical ramp rates $v_{0,\text{crit}}$ (a) and $v_{1,\text{crit}}$ (c) versus scaled B_0 offsets, $\tilde{\omega}_0$, and scaled B_1 amplitude, $\tilde{\omega}_1$. The right panels (b) and (d) show cross sections for $\omega_1 = \omega_{1,\text{nom}}$ of the two-dimensional graphs of the left panels (a) and (c). These cross sections are indicated as dashed lines on the left panels. The locations of the singularities, where the critical velocities vanish and the propagator becomes the unity operator [given by Eq. (46)], are marked by crosses on the left panels (a) and (c).

the scalable fast C++ simulation code developed by Colm Ryan and first described in Ref. [27]. The algorithm is based on the integration of the Bloch equations and allows a general pulse sequence with arbitrary and possibly time-dependent $\vec{B}_0(t)$ and $\vec{B}_1(t)$ fields. The simulations account for the effects of the rf pulses under possible off-resonance conditions and precession between the pulses in $\vec{B}_0(t)$. For the current results, we set the $1/T_1$ and $1/T_2$ relaxation rates to zero.

A. Linear ramp

We first present results for the simple case of a linear field ramp. It is assumed that at the start of the CPMG sequence, the B_0 field fulfills the Larmor condition. The deviation of the instantaneous Larmor frequency from the rf frequency is then of the form: $\omega_0(t)/\omega_{1,\text{nom}} = (d\tilde{\omega}_0/d\tau)t/t_E$. In practice, such a linear ramp can be caused by temporal fluctuations in the magnet or by motion of the sample relative to a magnetic field characterized by a gradient g . In that case with a relative velocity v , the dimensionless ramp rate is given by $d\tilde{\omega}_0/d\tau = \gamma g v t_E / \omega_{1,\text{nom}}$.

1. Simulation of magnetization

Figure 8 shows the results for five different ramp rates. For small offset frequencies, $\mathcal{A} \gg 1$ for all ramp rates. This implies that the spin dynamics starts in the adiabatic

regime for all cases. Furthermore, since the direction of the magnetization after the initial 90° pulse, M_{exc} , coincides with the eigenvector for the $k = 0$ (CPMG) mode, only this mode is initially occupied. Equation (32) then predicts that the magnetization follows \hat{n} : $\vec{M}(t) = \hat{n}[\tilde{\omega}_0(t)]$. In this regime, the magnetization is determined by the instantaneous offset frequency $\tilde{\omega}_0(t)$ and does not otherwise depend on the ramp rate. The simulation results in Fig. 8 at small to moderate offset frequencies are in full agreement with this prediction. The oscillations in M_x correspond to the variations in the direction of \hat{n} within the $\hat{x} - \hat{z}$ plane, as shown in Fig. 3. The magnetization is effectively spin locked to $\hat{n}(t)$, or equivalently to $\mathcal{B}_{\text{ave}}(t)$. At the highest ramp rate, a small \hat{y} component in \vec{M} becomes noticeable even at small offset frequencies. This is in agreement with Eq. (29) that shows that \hat{n} is slightly tilted from the $\hat{x} - \hat{z}$ plane. At the highest ramp rate of $d\tilde{\omega}_0/d\tau = 10^{-2}$, Eq. (29) predicts $\delta\varepsilon = 3.4^\circ$, which is in good agreement with the phase of the simulated magnetization at small values of $\tilde{\omega}_0$ in Fig. 8.

At the lowest ramp rate, the calculated adiabaticity parameter fulfills the adiabaticity condition $\mathcal{A} \gg 1$ at all offset frequencies considered. Therefore, the magnetization is predicted to follow Eq. (32) and to stay in the CPMG mode over the entire frequency range without any transition to the CP mode. This is confirmed in the simulations. At higher ramp rates, there are regions of offset frequencies where the adiabatic condition is not fulfilled

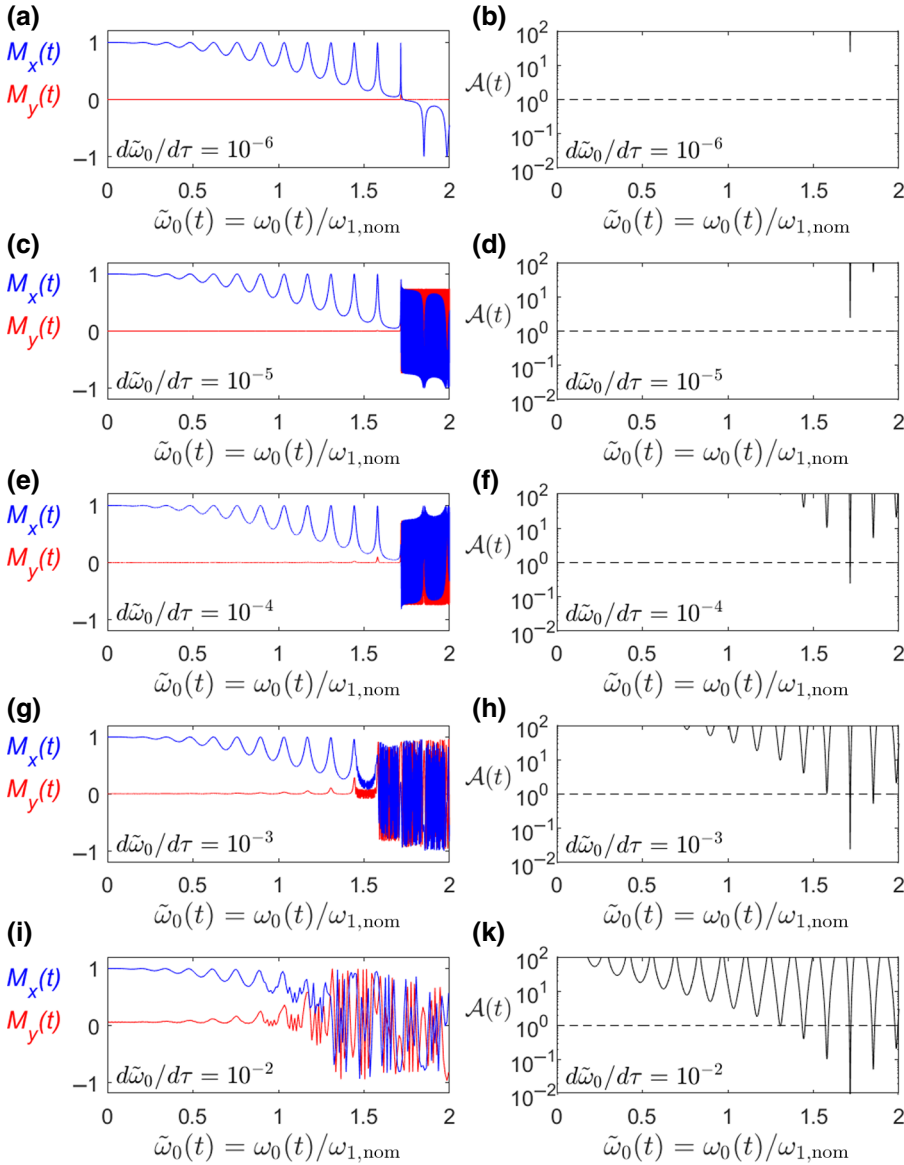


FIG. 8. Results for linear B_0 ramp starting from resonance with different ramp rates $d\tilde{\omega}_0/d\tau$ as indicated, $t_E/t_{180} = 15$, and $\omega_1 = \omega_{1,\text{nom}}$. The left panels [(a),(c),(e),(g), and (i)] show the simulation results of the transverse magnetization (blue, in phase; red, out of phase) as a function of the instantaneous offset frequency. The right panels [(b),(d),(f),(h), and (k)] show the calculated adiabaticity parameters \mathcal{A} , Eq. (42), as a function of the instantaneous offset frequency. The dashed line indicates $\mathcal{A} = 1$.

anymore. In these regions, the simulation results show indeed transitions between the CPMG and CP modes. The first onset is readily apparent in the simulations of Fig. 8 by the appearance of fast echo fluctuation and the appearance of large out-of-phase components. These features indicate a sizeable population of the CP modes. As predicted from the adiabaticity parameters displayed on the right panels, the appearance occurs at smaller offset frequencies when the ramp rate is increased.

2. Mode amplitudes

We can make this comparison between simulation and theory more quantitative by decomposing the magnetization obtained from the numerical simulation into the CPMG and CP components. Knowing the field fluctuation $\tilde{\omega}_0(t)$ allows us to calculate the eigenvectors $\hat{v}_k(t)$

from Eq. (17) to Eq. (19) for any time. The mode amplitudes $a_k(t)$ can then be extracted from the simulated magnetization data by $a_k(t) = \vec{M}(t) \cdot \hat{v}_k^*(t)$. The amplitude of the CPMG component corresponds to $a_0(t)$. The CP component consists of the $k = \pm 1$ modes and the corresponding amplitudes are, in general, fluctuating rapidly due to phase factors even in the adiabatic regime. However, the magnitude of the CP component, given by $|a_{\text{CP}}(t)| = \sqrt{2} |a_{\pm 1}(t)|$ is expected to be constant in the adiabatic regime.

Figure 9 displays the values of the CPMG amplitude and the CP magnitude extracted from the simulation as described. Superimposed to these results in gray scale are values of the adiabaticity parameter \mathcal{A} (same data as in the right panel of Fig. 8). The adiabatic and non-adiabatic region can be easily identified as white and dark sections, respectively. In the adiabatic regions, the

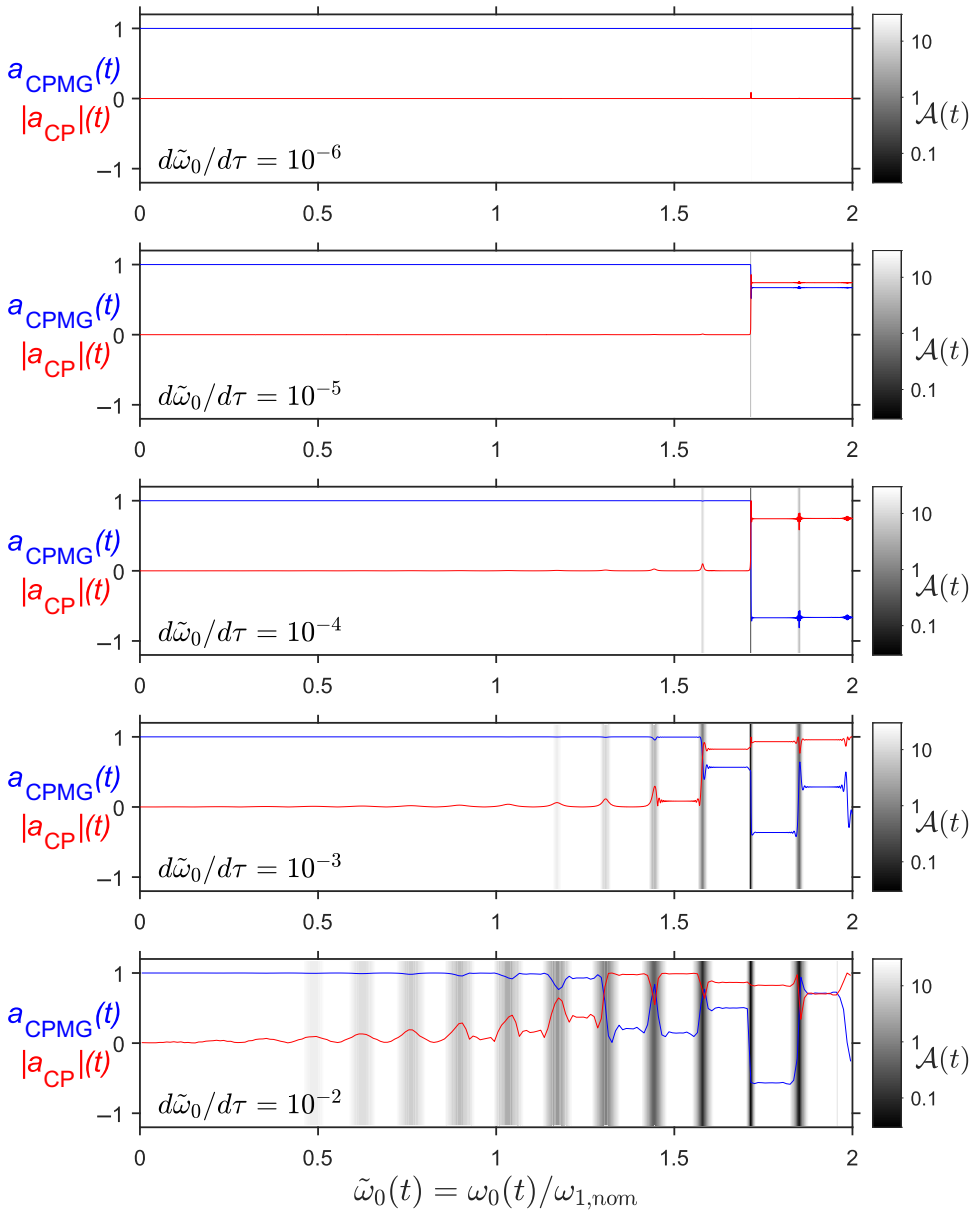


FIG. 9. CPMG amplitudes (blue) and CP magnitudes (red) extracted from the simulation results shown in Fig. 8 for the five different ramp rates as indicated. The instantaneous adiabaticity parameter $\mathcal{A}(t)$ is shown in gray scale. The white regions indicate adiabatic regions where the CPMG amplitudes and CP magnitudes stay constant.

extracted amplitude of the CPMG mode and the magnitude of the CP mode stay indeed constant and only change in the nonadiabatic regions. Until the first nonadiabatic region is reached, $a_{\text{CPMG}} = 1$. Figure 9 demonstrates that the adiabaticity parameter \mathcal{A} can accurately predict the onset of transitions between the CPMG and CP mode. Furthermore, it confirms the prediction that the number and extent of these nonadiabatic regions increases at higher ramp rates.

3. First-order corrections to analytical results

At modest ramp rates, it is interesting to observe the appearance and subsequent disappearance of M_y components in Fig. 8 and of the related CP amplitudes in Fig. 9. In the strictly adiabatic regime ($1/\mathcal{A} \rightarrow 0$), the evolution of

the magnetization is controlled by Eq. (32) and is expected to be

$$M_x^{(0)}(t) = \cos(\delta\epsilon)n_{\perp}(t), \quad (47)$$

$$|M_y^{(0)}(t)| = \sin(\delta\epsilon)n_{\perp}(t). \quad (48)$$

In this adiabatic limit, the magnitude of the M_y component is predicted to be bounded by $\sin(\delta\epsilon)$. In the linear displays of Figs. 8 and 9, deviations are clearly visible in regions with $1/\mathcal{A} \sim 0.1$. When M_y is displayed on a logarithmic scale (see Fig. 10), it is evident that there are systematic deviations even for much smaller values of $1/\mathcal{A}$. These deviations can be understood based on the inverted version of Eq. (38) [cf. Eq. (A10) in the Appendix]. A perturbation

calculation to first order in $1/\mathcal{A}$ yields

$$\begin{aligned}
 M_x^{(1)}(t) &= \frac{1}{\sqrt{1 + 1/\mathcal{A}(t)^2}} \\
 &\times [\cos(\delta\epsilon)n_{\perp}(t) - 1/\mathcal{A}(t)\sin(\delta\epsilon)], \\
 |M_y^{(1)}(t)| &= \frac{1}{\sqrt{1 + 1/\mathcal{A}(t)^2}} \\
 &\times [\sin(\delta\epsilon)n_{\perp}(t) + 1/\mathcal{A}(t)\cos(\delta\epsilon)].
 \end{aligned}
 \tag{49}$$

Here, the first terms come from the in-phase component that follows the adiabatic evolution. On the other hand, the second terms represent the out-of-phase component normal to the plane defined by \hat{z} and \hat{n} vectors, which drive the magnetization evolution away from the adiabatic trajectory. Comparisons of the simulation results and the first-order perturbation predictions shown in Fig. 10 demonstrate that the evolution of magnetizations during a linear-ramping process is essentially captured by the straightforward first-order perturbation calculations until a sizable transition occurs and the perturbation theory becomes invalid. At lower levels, we note discrepancies of $|M_y|$ between the simulation results and the perturbation predictions that are of the order of the dimensionless ramp rate $d\tilde{\omega}_0/d\tau$. These deviations can be attributed to the inherent discrete nature of the CPMG pulse sequence that is neglected in the average Hamiltonian picture.

It is feasible to extend the perturbation expansion to higher orders as described, for instance, in Ref. [28]. As discussed in the Appendix, Eq. (A10) describes the problem exactly in the continuous limit and can be solved numerically to give an exact answer.

4. Dependence of mode amplitudes on ramp rate

The results presented so far confirm that the adiabaticity parameter \mathcal{A} is able to predict the locations and the widths of the regions where transitions between the CPMG and CP modes can occur. However, the knowledge of \mathcal{A} is not sufficient to predict the change in the mode amplitude. As illustrated in Fig. 11, these changes are highly sensitive to the ramp rate.

Whenever a nonadiabatic region (delineated approximately by the red line) is encountered, the mode amplitude changes and assumes a new constant level in the next adiabatic region. A very small change in ramp rate can lead to a completely different level. The traversing of the nonadiabatic regions always lasts many refocusing cycles. Even small changes in the timing of the pulses can accumulate to large changes in the resulting magnetization. As a consequence, the robust prediction of the magnetization after traversing a nonadiabatic region is, in general, very challenging as it requires a very detailed knowledge of the field fluctuations that is often not available.

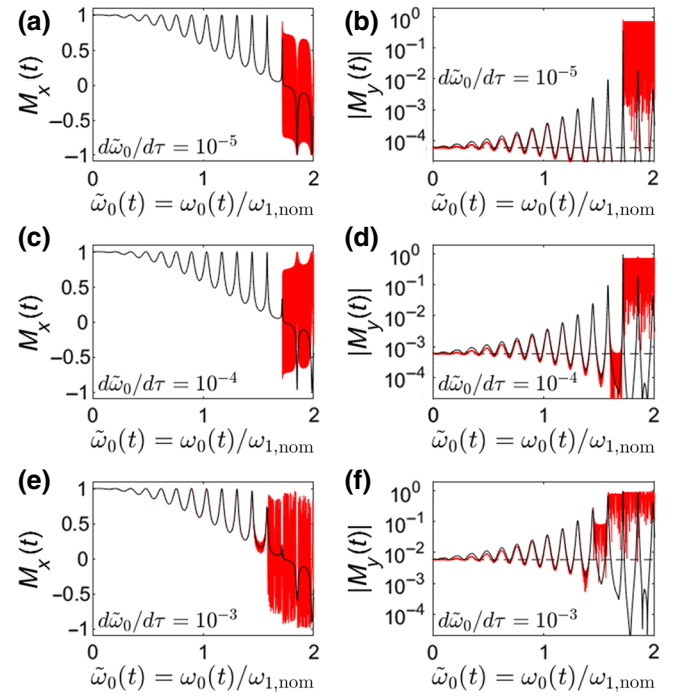


FIG. 10. Comparison of numerical simulations (red) with first-order analytical results (black) for the adiabatic regime as given by Eq. (49). The left panels [(a),(c), and (e)] show the in-phase magnetizations $M_x(t)$ and the right panels [(b),(d), and (f)] show the magnitude of the out-of-phase magnetizations $|M_y(t)|$ versus normalized offset frequency. The field ramp is assumed to be linear starting from resonance with a ramp rate $d\tilde{\omega}_0/d\tau$ as indicated. Furthermore, it is assumed that $t_E/t_{180} = 15$, and $\omega_1 = \omega_{1,nom}$. The black dashed line in the right panels shows the value of $\sin(\delta\epsilon)$.

B. Harmonic motion

The examples presented so far are characterized by linear field fluctuations with a constant ramp rate $d\tilde{\omega}_0/d\tau$. Here we demonstrate that the analysis developed in Sec. II applies to more general fluctuations with varying rates. The key quantity is the instantaneous adiabaticity parameter $\mathcal{A}(t)$ that controls whether the spin dynamics is in the adiabatic or nonadiabatic regime. This parameter is determined by the instantaneous offset frequency $\tilde{\omega}_0(t)$ and its instantaneous rate of change, $(d\tilde{\omega}_0/d\tau)(t)$. We can therefore characterize a particular B_0 fluctuation by its path in the $\tilde{\omega}_0 - d\tilde{\omega}_0/d\tau$ parameter space to determine the evolution of $\mathcal{A}(t)$. This approach is illustrated in Fig. 12 for harmonic motions.

The white areas in Fig. 12 indicate adiabatic regions, whereas the dark areas indicate nonadiabatic regions. If the path of the fluctuation is entirely confined to the white area [for example, the path labeled (a) in Fig. 12], then the spin dynamics is essentially adiabatic and Eq. (30) can be applied to lowest order. In this case, it is straightforward to predict the response of the system. The amplitude

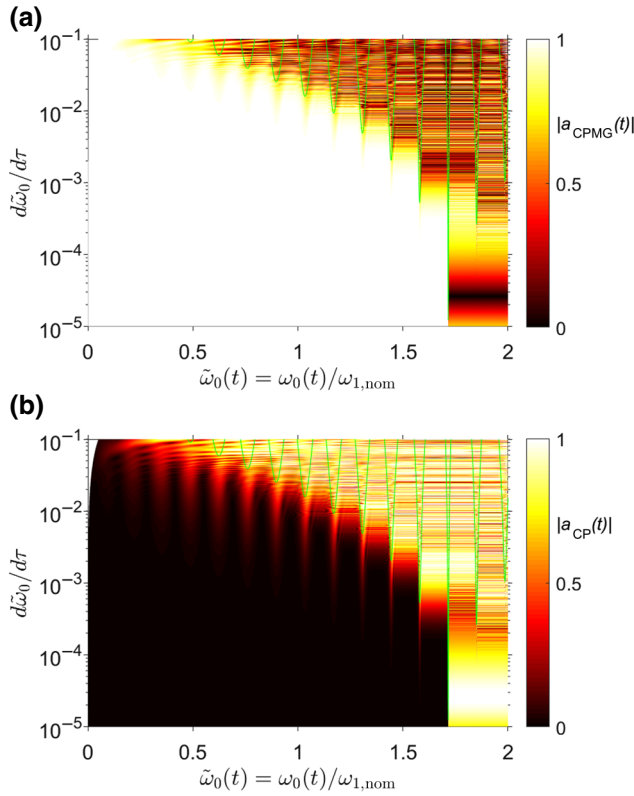


FIG. 11. Dependence of the eigenmode levels, extracted from the numerical simulations of the magnetization evolution during the CPMG, on instantaneous normalized field offset and ramp rate. Magnitudes of the CPMG mode (a) and CP mode (b) are displayed versus normalized offset frequency $\tilde{\omega}_0$ and ramp rate $d\tilde{\omega}_0/d\tau$ for linear field ramp starting from resonance. The green lines indicate the locations where $\mathcal{A}(t) = 2$. The simulations were performed for $t_E/t_{180} = 15$.

of the CPMG mode, a_{CPMG} , and the magnitude of the CP component, $|a_{\text{CP}}|$, stay constant. In contrast, when the path intersects nonadiabatic regions [e.g., path (c) in Fig. 12], transitions between the CPMG and CP modes occur and the behavior becomes very sensitive to the details of the path. We can accurately predict the onset of the chaotic behavior, but the prediction of the magnetization at later times becomes problematic as the response becomes extremely sensitive to the external parameters.

Figure 13 shows the time dependence of the magnetization and mode amplitudes obtained by numerical simulation for the three harmonic motions indicated in Fig. 12. The results for the longest period [path (a) in Fig. 12] show a purely in-phase magnetization that is periodic in time and synchronized with the fluctuation. The mode decomposition shows that the signal only contains the CPMG component. The magnetization is therefore perfectly spin locked to the instantaneous direction of \hat{n} and the evolution fully adiabatic. This simulation result is in full agreement with the simple analysis of its path in Fig. 12. The path

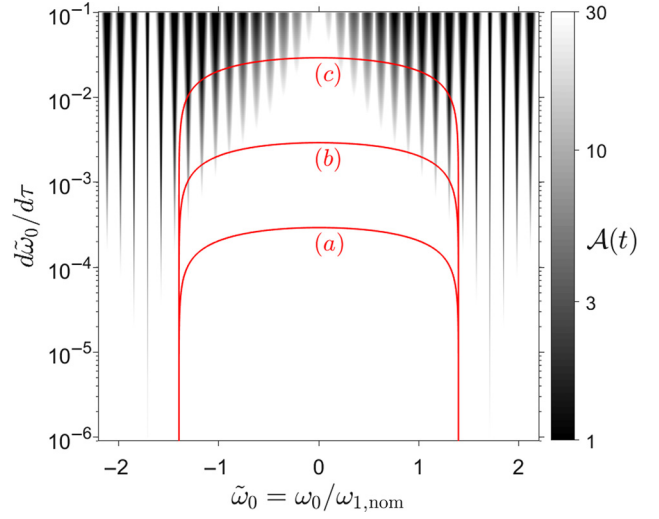


FIG. 12. Paths of harmonic fluctuations (red) superimposed over the adiabaticity parameter \mathcal{A} (shown in gray scale) in the $\tilde{\omega}_0 - d\tilde{\omega}_0/d\tau$ parameter space. The three harmonic motions are of the form $\omega_0(t) = \Delta\omega_0 \sin(2\pi t/T)$ with an amplitude of $\Delta\omega_0 = 1.4\omega_{1,\text{nom}}$ and periods T of (a) $T = 3 \times 10^4 t_E$, (b) $T = 3002 t_E$, and (c) $T = 300.2 t_E$. In all cases, $t_E/t_{180} = 15$.

(a) is completely confined to the adiabatic region with a minimum value of $\mathcal{A}(t)$ of $91 \gg 1$.

In contrast, the response for the shortest period T shown in Fig. 13(c) shows only a small region of adiabatic behavior similar to that in Fig. 13(a), but then becomes “noisy” and chaotic. The response is not periodic in time anymore. Again this is anticipated by the simple analysis of its path in Fig. 12. The minimum value of the adiabaticity parameter for path (c) is less than 1, clearly not fulfilling the adiabatic condition.

Finally, following the path (b) in Fig. 12, we observe the temporary generation and disappearance of M_y and hence of the $|a_{\text{CP}}|$ component in regions with $\mathcal{A} \sim 10$. Interestingly, the magnetization remains largely periodic under the harmonic fluctuation without inducing strong irreversible transitions. This phenomenon is consistent with the observation in the linear-ramping case and can be explained similarly by the first-order correction given in Eq. (49). In such a case, no “true” nonadiabatic transition is induced.

C. Return to the origin

An important class of field fluctuations are cyclic where after some time T , the field returns to its original value at $t = 0$. Examples include the harmonic field fluctuations considered in the previous section.

As the field returns to its original value, the magnetization generated by the CPMG sequence does, in general, not recover its original value (neglecting relaxation effects). However, there is an important exception: the CPMG component of the magnetization recovers its initial value if

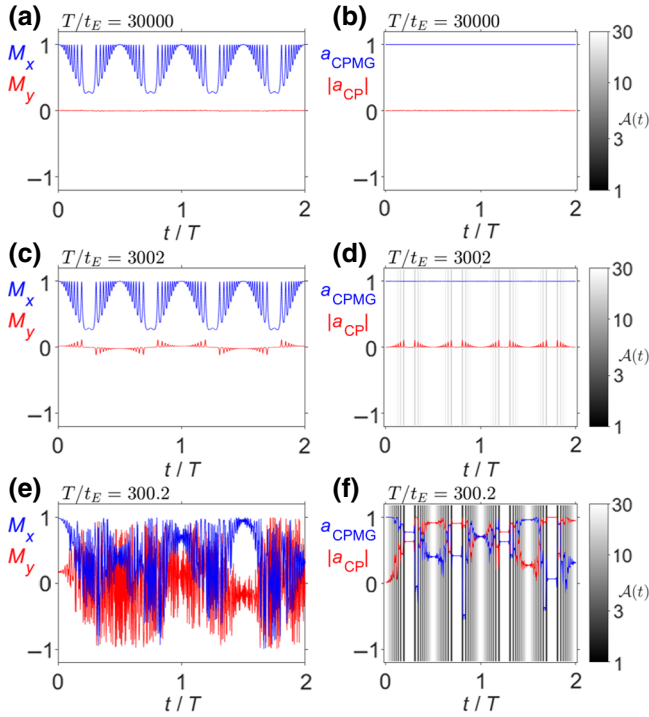


FIG. 13. Results for harmonic field variations $B_0(t)$ with an amplitude of $1.4 B_1$ starting from resonance. The left panels [(a),(c), and (e)] show the resulting transverse magnetization over two periods (blue, in-phase; red, out of phase). The right panels [(b),(d), and (f)] show the extracted CPMG amplitudes (blue) and CP magnitudes (red). The instantaneous adiabaticity parameter $\mathcal{A}(t)$ are shown in gray scale. The period T is varied from $T = 3 \times 10^4 t_E$ [(a) and (b)] to $T = 3002 t_E$ [(c) and (d)] and $T = 300.2 t_E$ [(e) and (f)]. For the three values of T , the minimum adiabaticity parameters are 91, 9.1, and 0.93, respectively. In all cases, $t_E/t_{180} = 15$.

the path of the field fluctuation is confined to an adiabatic region of the phase diagram. This is, for instance, the case for path (a) in Fig. 12. Indeed, the magnetization shown in Fig. 13(a) periodically recovers its full initial value at times when the field returns to its initial value. This is not observed consistently for path (c), as the path now crosses nonadiabatic regions of the phase diagram.

We explore this effect more systematically for the case of a bilinear field variation with results presented in Figs. 14 and 15. Here we assume a linear field ramp from $\omega_{0,\text{start}}$ to $\omega_{0,\text{peak}}$, followed by an reverse ramp back from $\omega_{0,\text{peak}}$ to $\omega_{0,\text{start}}$. We assume that the magnitudes of the ramp rates are fixed at $|d\tilde{\omega}_0/d\tau| = 10^{-3}$. The total duration of the field excursion, T , is then $T/t_E = 2 |(\omega_{0,\text{peak}} - \omega_{0,\text{start}})/\omega_{1,\text{nom}}| / |d\tilde{\omega}_0/d\tau|$.

In Fig. 14, we present the transverse magnetization at the end of the ramps, $M_x(T)$, as a function of the starting and peak values of the offset frequency, $\omega_{0,\text{start}}$ and $\omega_{0,\text{peak}}$, respectively. At time T , the offset frequency has returned to

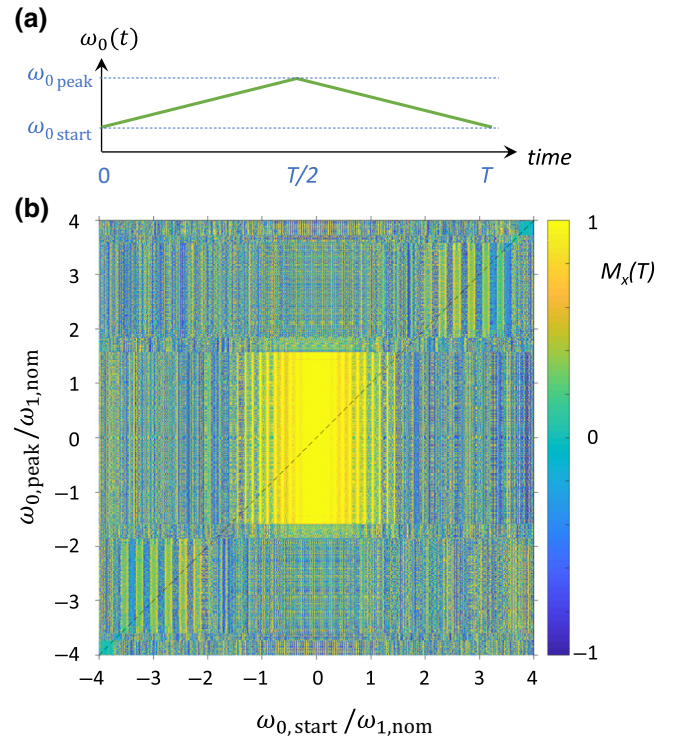


FIG. 14. Return to the origin field fluctuations. Panel (a) shows the B_0 field fluctuations considered here: a linear ramp from $\omega_{0,\text{start}}$ to $\omega_{0,\text{peak}}$ followed by a reverse ramp back to $\omega_{0,\text{start}}$. The ramp rate is assumed to be $|d\tilde{\omega}_0/d\tau| = 10^{-3}$. The main panel (b) shows the resulting in-phase magnetization $M_x(t = T)$ at the end of the ramps as a function of $\omega_{0,\text{start}}$ and $\omega_{0,\text{peak}}$. The dashed line indicates the diagonal where $\omega_{0,\text{start}} = \omega_{0,\text{peak}}$ and no field variation occurred during the CPMG sequence. The simulation assumed $t_E/t_{180} = 15$.

its starting value: $\omega_0(T) = \omega_{0,\text{start}}$. The field variation during the ramp is $\omega_{0,\text{peak}} - \omega_{0,\text{start}}$, i.e., the vertical distance of the point of interest from the diagonal shown as the dashed line.

The results in Fig. 14 show vertical striplike structures in square regions along the diagonal with a superposition of some noiselike features. The noiselike features are caused by contributions from the CP mode to $M_x(T)$. Even if the fluctuations explore purely adiabatic regions of the phase space, the magnetization of the CP component, $M_{\text{CP}}(T)$, is highly sensitive to the exact path taken. This is evident from the phase factor $\exp\left\{-\frac{i}{\hbar} \int_0^t E_k(t') dt' + i\Gamma_k(t)\right\}$ in Eq. (36).

For $\omega_{0,\text{start}} \neq 0$, CP contributions are generated at the start of the CPMG sequence. Even for fully adiabatic field fluctuations, the total magnetization then exhibits a noticeable path sensitivity through the CP contribution. We can simplify the analysis of Fig. 14 by analyzing only the CPMG component of $M_x(T)$. In Fig. 15, we present

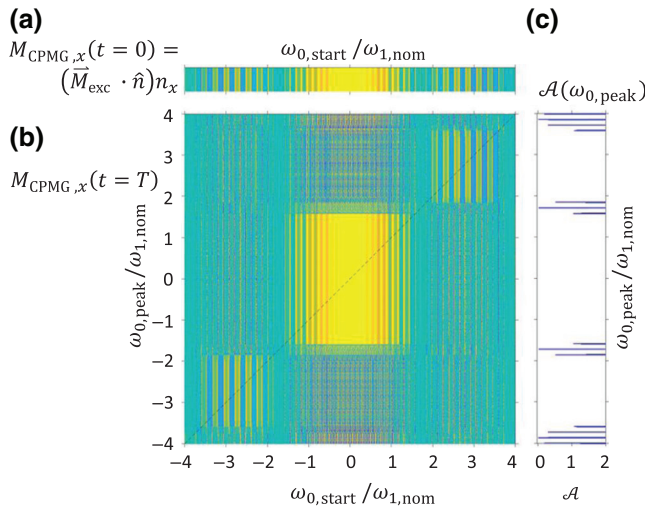


FIG. 15. The main panel (b) shows the in-phase CPMG component, $M_{\text{CPMG},x}(t = T)$ as a function of normalized start and peak offset. These results are obtained from the simulations shown in Fig. 14. The top panel (a) shows the calculated initial CPMG magnetization $M_{\text{CPMG},x}(t = 0)$, whereas (c) shows the adiabaticity parameter \mathcal{A} as a function of offset frequency.

$M_{\text{CPMG},x}(t = T)$ that was obtained by projecting $\vec{M}(T)$ onto $\hat{n}(T)$.

The square regions along the diagonal now stand out clearly and they are free of noiselike features. Within each square, the magnetization is uniform along the $\omega_{0,\text{peak}}$ dimension. The central square extends from $\pm 1.58\omega_{1,\text{nom}}$, whereas the satellite squares are positioned from $\pm (1.85 \text{ to } 3.59)\omega_{1,\text{nom}}$ along both the $\omega_{0,\text{start}}$ and $\omega_{0,\text{peak}}$ dimensions. These ranges correspond exactly to the adiabatic regions for $|d\tilde{\omega}_0/d\tau| = 10^{-3}$, as shown by the adiabaticity parameter \mathcal{A} displayed on the right of Fig. 15. In these regions, the spin dynamics is fully adiabatic and the CPMG component is fully reversible, i.e., $\vec{M}_{\text{CPMG}}(t = T) = \vec{M}_{\text{CPMG}}(t = 0)$. Its amplitude is given by $(\vec{M}_{\text{exc}} \cdot \hat{n}) \hat{n}$. The calculations of this initial amplitude of the CPMG component are shown on the top of Fig. 15.

Outside the square regions, there are still noiselike features present. This indicates that the CPMG magnetization detected at $t = T$ has contributions from the CP mode with at least one mode transition during T . In general, the paths of the corresponding field fluctuations' traverse nonadiabatic regions where the adiabatic condition $\mathcal{A} \gg 1$ is not fulfilled.

The full simulation of the different field fluctuations shown in Fig. 14 is computationally expensive. However, the results presented here demonstrates that the key features can be readily obtained from the analytical results with minimal computational effort. The determination of the boundaries of the special square regions requires the calculation of $\mathcal{A}(\omega_{0,\text{peak}})$, a property of a single refocusing cycle. The amplitudes of the magnetization within the

special regions in turn requires only the simple calculation of the initial amplitude of the CPMG mode, determined by $\vec{M}_{\text{exc}}(\omega_{0,\text{start}})$ and $\hat{n}(\omega_{0,\text{start}})$.

IV. CONCLUSION

We develop the theoretical framework to analyze the spin dynamics of the CPMG sequence with fluctuating magnetic fields. In many applications, temporal variations of the external field are an unavoidable nuisance caused by noise or by motion between the sample and the sensor. It is important to assess the impact that such fluctuations have on the intended use of the CPMG sequence to repeatedly refocus the magnetization. This work provides the necessary tool.

The analysis is based on the decomposition of the magnetization into eigenmodes of the refocusing cycle. One of the eigenmodes (labeled CPMG mode) is always associated with eigenvalue 1, whereas the other modes (labeled CP modes) have eigenvalues of the form $e^{\pm i\alpha}$, where the angle α depends on the off-resonance condition characterized by the normalized offset frequency $\tilde{\omega}_0$. We introduce the adiabaticity parameter \mathcal{A} that is the ratio of the critical velocity $v_{0,\text{crit}}(\tilde{\omega}_0)$ and the normalized rate of change of the magnetic field, $d\tilde{\omega}_0/d\tau$. The spin dynamics is adiabatic without any transitions between the CPMG and CP modes when the adiabatic condition $\mathcal{A} \gg 1$ is fulfilled. There are simple analytical solutions in this regime. Otherwise, mode transitions can occur and the response becomes chaotic. Field fluctuations can be characterized by their path in the $\tilde{\omega}_0 - d\tilde{\omega}_0/d\tau$ plane to predict the range of the adiabatic regime and the onset of the chaotic behavior associated with the nonadiabatic regime. The theoretical analysis is extensively tested with numerical simulations. We also outline the extension of this analysis of B_0 fluctuations to joint $B_0 - B_1$ fluctuations.

For the standard CPMG sequence, the adiabaticity parameter (and the critical velocities) show pronounced minima at offset frequencies close to $\pm\sqrt{3}\omega_{1,\text{nom}}$, $\pm\sqrt{15}\omega_{1,\text{nom}}, \dots$. This behavior is caused by close-by degeneracies between the CPMG and CP modes. It is difficult to pass through the neighborhood of degenerate points without entering the nonadiabatic regime that results in a chaotic response.

The analysis is based on the general properties of the propagator of a single refocusing cycle. Here we consider the simplest possible refocusing cycle containing a single pulse, but this approach is applicable to more general cases that incorporate composite pulses [29–31] or frequency sweeps [21,32]. This also opens the possibility to design optimized refocusing pulses that are more robust to B_0 and or B_1 fluctuations than the standard pulses. The key criterium is to design refocusing sequences that have no singular points close to the range of operations, i.e., to

avoid extreme minima in the critical velocities $v_{0,\text{crit}}$ and $v_{1,\text{crit}}$.

The present approach can be considered as a generalization of the standard technique of decomposing the magnetization into different coherence pathways [33,34]. In the standard approach, the magnetization is decomposed into the eigenmodes of free precession. Since every refocusing pulse can induce transitions, it is essential to keep track of the coherence in each refocusing cycle. This makes this approach impractical as the number of relevant coherence pathways grows exponentially with echo number. The current approach avoids this divergence of coherence pathways. Rather than using the eigenmodes of free precession, we perform here a decomposition into the eigenmodes of the refocusing cycle. We only have to consider transitions between the different adiabatic regions that are separated by regions where the adiabatic condition $\mathcal{A} \gg 1$ is not fulfilled. The adiabatic regions typically extend over a large number of refocusing cycles, which results in a large decrease of relevant coherence pathways.

The transition rates between the different adiabatic regimes are highly sensitive to the external parameters such as ramp rates. This implies that when transitions between the CP and CPMG levels occur, the outcome of an experiment on a single spin is difficult to predict in a robust manner. There is no problem calculating the transition rates numerically, but it is challenging to determine the actual external parameters sufficiently accurately.

APPENDIX: TRANSITION BETWEEN CPMG AND CP MODES IN THE CONTINUOUS LIMIT

In this Appendix, we provide a brief review on the derivation of Eq. (38), following closely those in Ref. [26], and then discuss how to use the inverted form of Eq. (38) to compute the transition rate between different eigenstates.

1. Derivation of Eq. (38)

Let us consider an arbitrary time-dependent Hamiltonian, $\mathcal{H}_0(t)$, that has the instantaneous eigenstates, $|u_\ell(t)\rangle$, with energies $E_\ell(t)$. In the adiabatic approximation, the evolution of states is given by

$$|\psi_\ell(t)\rangle = \exp \left\{ -\frac{i}{\hbar} \int dt' E_\ell(t') - \int dt' \langle u_\ell(t') | \partial_{t'} u_\ell(t') \rangle \right\} |u_\ell(t)\rangle. \quad (\text{A1})$$

The first integral inside the exponential is simply the dynamic phase while the second one related to the geometric phase accumulated by the time-dependent state. This adiabatic time evolution of all states can be defined by a

time-dependent unitary operator expressed by

$$U(t) = \sum_\ell \exp \left\{ -\frac{i}{\hbar} \int dt' E_\ell(t') - \int dt' \langle u_\ell(t') | \partial_{t'} u_\ell(t') \rangle \right\} |u_\ell(t)\rangle \langle u_\ell(0)|. \quad (\text{A2})$$

Interestingly, there exists a modified Hamiltonian $\mathcal{H}_{\text{mod}}(t)$ that gives rise to this exact time-dependent unitary operator in the general case, not just in the adiabatic limit. It can be shown that this modified Hamiltonian $\mathcal{H}_{\text{mod}}(t)$ can be formally expressed as

$$\mathcal{H}_{\text{mod}} = i\hbar [\partial_t U(t)] U^\dagger(t), \quad (\text{A3})$$

where the symbol \dagger indicates the Hermitian conjugate of the operator. Explicitly, this constructed Hamiltonian can be written as

$$\begin{aligned} \mathcal{H}_{\text{mod}}(t) &= \sum_\ell E_\ell(t) |u_\ell\rangle \langle u_\ell| \\ &+ i\hbar \sum_\ell (|\partial_t u_\ell\rangle \langle u_\ell| - \langle u_\ell | \partial_t u_\ell\rangle |u_\ell\rangle \langle u_\ell|) \\ &\equiv \mathcal{H}_0(t) + \mathcal{H}_1(t). \end{aligned} \quad (\text{A4})$$

Here, all the bra and ket states are evaluated at time t . The first summation simply gives $\mathcal{H}_0(t)$ as the original Hamiltonian while the second summation is grouped into $\mathcal{H}_1(t)$ as the additional term required for driving eigenstates to follow the adiabatic evolution in Eq. (A1).

The additional part of Hamiltonian $\mathcal{H}_1(t)$ can be rewritten into the form

$$\mathcal{H}_1(t) = i\hbar \sum_{\ell' \neq \ell} \sum \frac{|u_{\ell'}\rangle \langle u_{\ell'} | \partial_t H_0 | u_\ell\rangle \langle u_\ell|}{E_\ell - E_{\ell'}}, \quad (\text{A5})$$

with the aid of the identity

$$\langle u_{\ell'} | \partial_t u_\ell \rangle = \frac{\langle u_{\ell'} | \partial_t H_0 | u_\ell \rangle}{E_\ell - E_{\ell'}}. \quad (\text{A6})$$

It is worthwhile to point out that the above procedure can be utilized to construct the exactly driving Hamiltonian $\mathcal{H}_{\text{mod}}(t)$ for any time-dependent Hamiltonian $\mathcal{H}_0(t)$ without generating transition between them.

We can now compute the exact driving Hamiltonian $\mathcal{H}_{\text{mod}}(t)$ for the original time-dependent Hamiltonian given in Eq. (34), $\mathcal{H}_0(t) = \mathcal{H}_{\text{ave}}(t)$. From the expression of H_1 in

Eq. (A5), we have

$$\mathcal{H}_1(t) = i\hbar^2\gamma [\partial_t \mathcal{B}_{\text{ave}}(t)] \cdot \sum_{\ell' \neq \ell} \sum_{\ell} \frac{|u_{\ell'}\rangle \langle u_{\ell'}| \vec{\mathcal{S}} |u_{\ell}\rangle \langle u_{\ell}|}{E_{\ell} - E_{\ell'}}. \quad (\text{A7})$$

After some algebra following Ref. [26], one can cast Eq. (A7) into the concise expression:

$$\mathcal{H}_1(t) = \frac{\hbar}{|\mathcal{B}_{\text{ave}}(t)|^2} \mathcal{B}_{\text{ave}}(t) \times \partial_t \mathcal{B}_{\text{ave}}(t) = \hbar \hat{n}(t) \times \partial_t \hat{n}(t). \quad (\text{A8})$$

The exact driving Hamiltonian can now be written as

$$\begin{aligned} \mathcal{H}_{\text{mod}}(t) &= \mathcal{H}_0(t) + \mathcal{H}_1(t) = \hbar [\gamma \mathcal{B}_{\text{ave}} + \hat{n}(t) \times \partial_t \hat{n}(t)] \cdot \vec{\mathcal{S}} \\ &\equiv \hbar \gamma \mathcal{B}_{\text{mod}} \cdot \vec{\mathcal{S}}. \end{aligned} \quad (\text{A9})$$

This gives the modified effective B field given in Eq. (38).

2. Inverted interpretation and transition rate

The exact driving Hamiltonian $\mathcal{H}_{\text{mod}}(t)$ in Eq. (A9) is derived knowing both the original Hamiltonian $\mathcal{H}_0(t)$ and its corresponding adiabatic evolution states. Interestingly, for a spin coupled to the magnetic field, it also provides a way to compute the exact evolution driven by the original Hamiltonian, $\mathcal{H}_{\text{ave}}(t)$ beyond the adiabatic limit, i.e., compute the exact time-dependent eigenstates driven by the original Hamiltonian, $\mathcal{H}_{\text{ave}}(t)$. More precisely, Eq. (38) can be used to read

$$\gamma \mathcal{B}_{\text{ave}}(t) = [\gamma \mathcal{B}_{\text{eff}}(t) + \hat{n}_{\text{eff}}(t) \times \partial_t \hat{n}_{\text{eff}}(t)], \quad (\text{A10})$$

where $\hat{n}_{\text{eff}}(t) \equiv \mathcal{B}_{\text{eff}}(t)/|\mathcal{B}_{\text{eff}}(t)|$. We are searching for an effective field $\mathcal{B}_{\text{eff}}(t)$ such that its modified field $\mathcal{B}_{\text{mod}}(t)$ is identical to the original field $\mathcal{B}_{\text{ave}}(t)$. The direction vector $\hat{n}_{\text{eff}}(t)$ then corresponds to the exact eigenstate driven by $\mathcal{H}_{\text{ave}}(t)$. The task now reduces to solving the coupled differential equations Eq. (A10) for each component of \mathcal{B}_{eff} and $\hat{n}_{\text{eff}}(t)$. The general form for the magnetization has then the form of Eq. (36), even outside the adiabatic limit. In particular, for the important case when $\vec{M}_{\text{exc}} = \hat{n}_{\text{eff}}(t=0)$, the solution reduces to the simple form $\vec{M}(t) = \hat{n}_{\text{eff}}(t)$.

In principle, Eq. (A10) applies to any spin system coupled to a well-defined and continuous magnetic field. For the specific problem on our hand, there are two caveats worth to keep in mind. First, the effective magnetic field, $\mathcal{B}_{\text{ave}}(t) = [\alpha(t)/t_E] \hat{n}(t)$, is derived from the analysis of the rotation operation on the magnetization at each refocusing cycle. However, the direction of the rotation axis is only defined modulo a factor of -1 . Following the convention in the main text, we constrained the effective rotation angle to $0 \leq \alpha \leq \pi$. This can lead to discontinuities in the direction of \mathcal{B}_{ave} when α approaches π and the corresponding

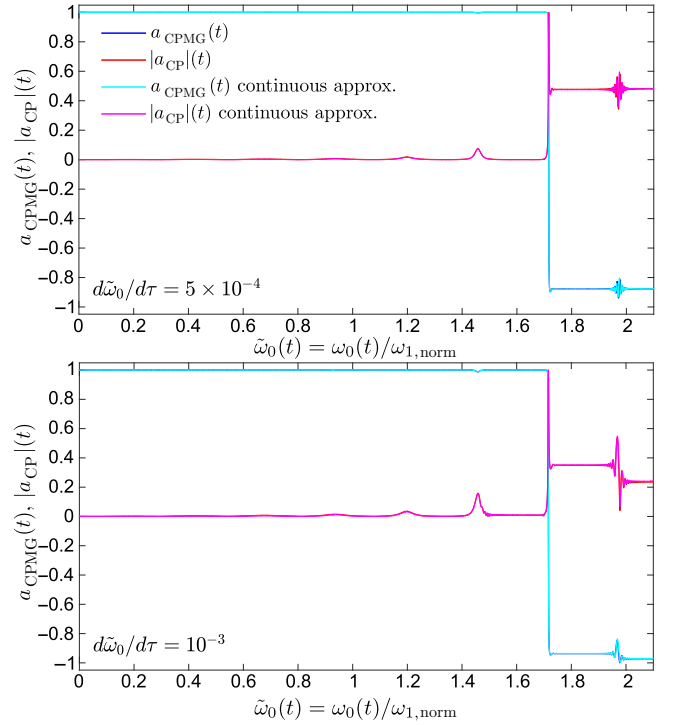


FIG. 16. CPMG amplitudes and CP magnitudes obtained from the direct spin-dynamics simulation (red and blue curves) and from the continuous approximation (cyan and magenta curves). The two panels show simulation results for two ramp rates, $d\tilde{\omega}_0/d\tau = 5 \times 10^{-4}$ and 10^{-3} , and $t_E/t_{180} = 8$, respectively.

rotating direction $\hat{n}(t)$ switches between opposite directions. Hence, for using Eq. (A10) to evaluate the evolution of state or transition rate with time-dependent fields, we need to solve it piece wisely between the discontinuous points and to project eigenstates into the new basis at the discontinuous points.

Second, we treat the effective magnetic field, $\mathcal{B}_{\text{ave}}(t)$ as the continuous representation of the discrete rotations generated by each refocusing cycle. When the applied magnetic field B_0 and/or the pulsed field B_1 vary too fast, this continuous approximation may not be fully justified. Although the qualitative properties, such as occurrences of mode transitions, can still be understood, one should not expect to obtain quantitative results from the continuous formalism in those cases.

In Sec. III, we use Eq. (A10) together with the first-order perturbation calculation to obtain Eq. (49) that explains the variations of the magnetization $|M_y|$ in the linear-ramping process up to the nonadiabatic region. Equation (A10), however, is quite general and allows us to faithfully capture the transition between CPMG and CP modes in the nonadiabatic region. We test this approach of calculating the spin dynamics based on solving Eq. (A10) by comparing the results with those based on the standard numerical integration of the Bloch equation used in generating the

results presented in Sec. III. Figure 16 shows comparisons for simulations of linear field fluctuations with two different ramp rates. The calculations assumed that at the start of the ramp $\tilde{\omega}_0(t=0) = 0$ and that the magnetization was initially all in the CPMG mode, $a_{\text{CPMG}}(t=0) = 1$. The refocusing cycle duration is eight times of the pulse width, $t_E/t_{180} = 8$. Figure 16 displays the evolution of the amplitudes of CPMG and CP modes calculated by the two approaches. The results from the two approaches nearly coincide, thus validating the alternative method based on the continuous approximation and Eq. (A10). Only small discrepancies can be observed. All the primary features and even the quantitative values of amplitudes of CPMG and CP modes from the continuous approximation are comparable to those obtained from direct spin-dynamics simulation.

-
- [1] F. Casanova, J. Perlo, and B. Blümich, eds., *Single-Sided NMR* (Springer, Berlin, Heidelberg, 2011).
- [2] M. D. Hürlimann and N. J. Heaton, in *Mobile NMR and MRI: Developments and Applications* (Royal Society of Chemistry, Cambridge, 2015), p. 11.
- [3] H. Y. Carr and E. M. Purcell, Effects of diffusion on free precession in nuclear magnetic resonance experiments, *Phys. Rev.* **94**, 630 (1954).
- [4] S. Meiboom and D. Gill, Modified spin-echo method for measuring nuclear relaxation times, *Rev. Sci. Instrum.* **29**, 688 (1958).
- [5] K. Lim, T. Nguyen, T. Mazur, D. E. Wemmer, and A. Pines, Sensitivity enhancement in multiple-quantum NMR experiments with CPMG detection, *J. Magn. Reson.* **157**, 160 (2002).
- [6] M. D. Hürlimann and L. Venkataramanan, Quantitative measurement of two-dimensional distribution functions of diffusion and relaxation in grossly inhomogeneous fields, *J. Magn. Reson.* **157**, 31 (2002).
- [7] P. Cappellaro, J. S. Hodges, T. F. Havel, and D. G. Cory, Principles of control for decoherence-free subsystems, *J. Chem. Phys.* **125**, 044514 (2006).
- [8] M. J. Biercuk, H. Uys, A. P. VanDevender, N. Shiga, W. M. Itano, and J. J. Bollinger, Optimized dynamical decoupling in a model quantum memory, *Nature* **458**, 996 (2009).
- [9] P. Speier, S. Crary, R. L. Kleinberg, and C. Flaum, in *Trans. SPWLA 40th Annual Logging Symposium* (Society of Professional Well Log Analysts (SPWLA), Oslo, 1999), Paper II.
- [10] A. E. Dementyev, D. Li, K. MacLean, and S. E. Barrett, Anomalies in the NMR of silicon: Unexpected spin echoes in a dilute dipolar solid, *Phys. Rev. B* **68**, 153302 (2003).
- [11] U. Haeberlen and J. S. Waugh, Coherent averaging effects in magnetic resonance, *Phys. Rev.* **175**, 453 (1968).
- [12] R. R. Ernst, G. Bodenhausen, and A. Wokaun, *Principles of Nuclear Magnetic Resonance in One and Two Dimensions* (Clarendon Press, Oxford, 1987).
- [13] M. D. Hürlimann and D. D. Griffin, Spin dynamics of Carr-Purcell-Meiboom-Gill-like sequences in grossly inhomogeneous B_0 and B_1 fields and application to NMR well logging, *J. Magn. Reson.* **143**, 120 (2000).
- [14] L. Landau, Zur Theorie der Energieübertragung. II, *Phys. Z. Sowjetunion* **2**, 46 (1932).
- [15] C. Zener, Non-adiabatic crossing of energy levels, *Proc. R. Soc. London A* **137**, 696 (1932).
- [16] B. Blümich and H. Spiess, Quaternions as a practical tool for the evaluation of composite rotations, *J. Magn. Reson.* **61**, 356 (1985).
- [17] C. Counsell, M. H. Levitt, and R. R. Ernst, Analytical theory of composite pulses, *J. Magn. Reson.* **63**, 133 (1985).
- [18] D. J. Siminovitch, Rotations in NMR: Part I. Euler-Rodrigues parameters and quaternions, *Concepts Magn. Reson.* **9**, 149 (1997).
- [19] M. Born and V. Fock, Beweis des Adiabatsatzes, *Z. Phys.* **51**, 165 (1928).
- [20] M. V. Berry, Quantal phase factors accompanying adiabatic changes, *Proc. R. Soc. Lond. A* **392**, 45 (1984).
- [21] M. Garwood and L. Delabarre, The return of the frequency sweep: Designing adiabatic pulses for contemporary NMR, *J. Magn. Reson.* **153**, 155 (2001).
- [22] J. Baum, R. Tycko, and A. Pines, Broadband and adiabatic inversion of a two-level system by phase modulated pulses, *Phys. Rev. A* **32**, 3435 (1985).
- [23] A. Tannús and M. Garwood, Adiabatic pulses, *NMR Biomed.* **10**, 423 (1997).
- [24] E. C. G. Stueckelberg, Theorie der unelastischen Stöße zwischen Atomen, *Helv. Phys. Acta* **5**, 369 (1932).
- [25] E. Majorana, Atomi orientati in campo magnetico variabile, *Il Nuovo Cimento* (1924–1942) **9**, 43 (1932).
- [26] M. V. Berry, Transitionless quantum driving, *J. Phys. A: Math. Theor.* **42**, 365303 (2009).
- [27] C. Duan, C. Ryan, S. Utsuzawa, Y. Q. Song, and M. D. Hürlimann, Effect of off-resonance on T_1 saturation recovery measurement in inhomogeneous fields, *J. Magn. Reson.* **281**, 31 (2017).
- [28] M. Deschamps, G. Kervern, D. Massiot, G. Pintacuda, L. Emsley, and P. J. Grandinetti, Superadiabaticity in magnetic resonance, *J. Chem. Phys.* **129**, 204110 (2008).
- [29] M. D. Hürlimann, Carr-Purcell sequences with composite pulses, *J. Magn. Reson.* **152**, 109 (2001).
- [30] T. W. Borneman, M. D. Hürlimann, and D. G. Cory, Application of optimal control to CPMG refocusing pulse design, *J. Magn. Reson.* **207**, 220 (2010).
- [31] S. Mandal, V. D. M. Koroleva, T. W. Borneman, Y.-Q. Song, and M. D. Hürlimann, Axis-matching excitation pulses for CPMG-like sequences in inhomogeneous fields, *J. Magn. Reson.* **237**, 1 (2013).
- [32] R. W. Schurko, Ultra-wideline solid-state NMR spectroscopy, *Acc. Chem. Res.* **46**, 1985 (2013).
- [33] R. Kaiser, E. Bartholdi, and R. R. Ernst, Diffusion and field-gradient effects in NMR Fourier spectroscopy, *J. Chem. Phys.* **60**, 2966 (1974).
- [34] G. Bodenhausen, H. Kogler, and R. Ernst, Selection of coherence transfer pathways in NMR pulse experiments, *J. Magn. Reson.* **58**, 370 (1984).